CHALMERS
UNIVERSITY OF TECHNOLOGY

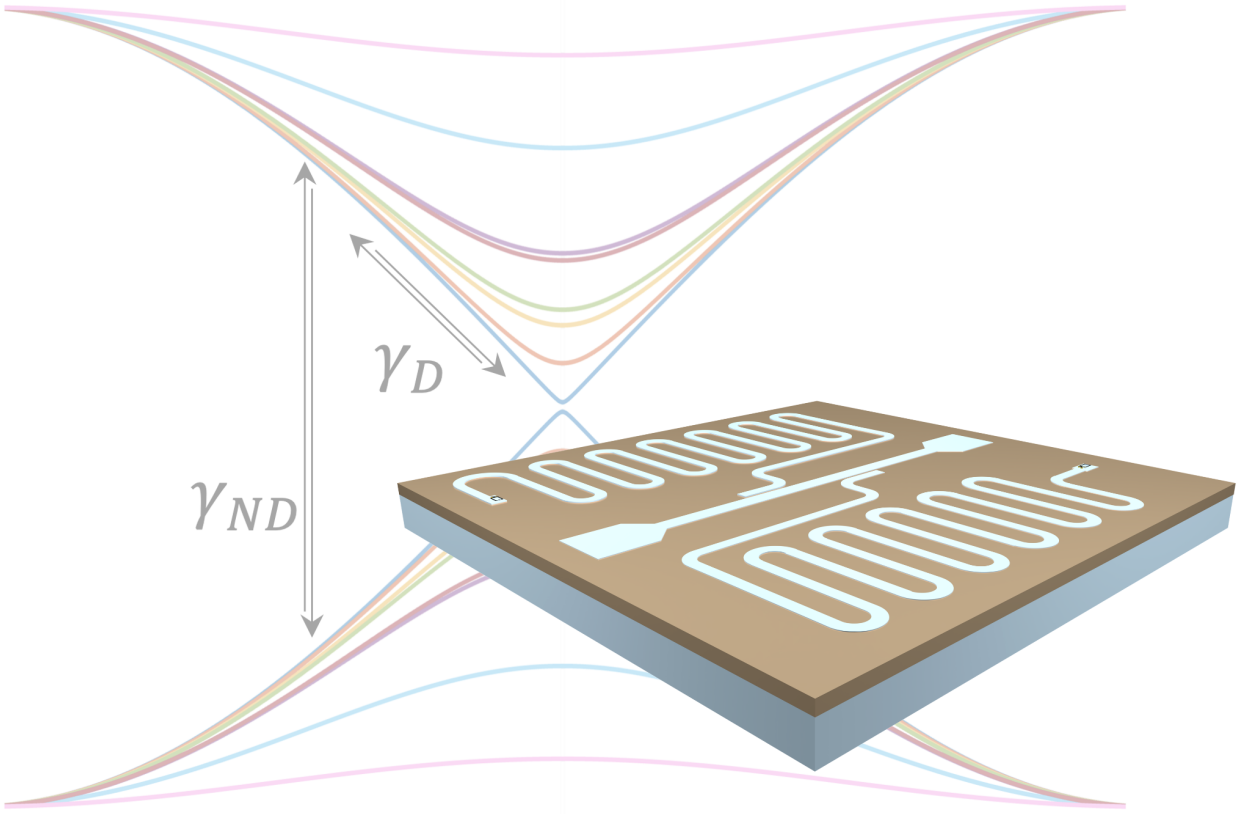

Towards probing zero energy bound states with circuit QED in topological insulator junctions

Master thesis in Nanotechnology

NÚRIA ALCALDE HERRAIZ

DEPARTMENT OF MICROTECHNOLOGY AND NANOSCIENCE
CHALMERS UNIVERSITY OF TECHNOLOGY
Gothenburg, Sweden 2023
www.chalmers.se

Master's thesis 2023

Towards probing zero energy bound states with circuit QED in topological insulator junctions

NÚRIA ALCALDE HERRAIZ

CHALMERS
UNIVERSITY OF TECHNOLOGY

Department of Microtechnology and Nanoscience - MC2
Quantum Device Physics Laboratory - QDP
Chalmers University of Technology
Gothenburg, Sweden 2023

Towards probing zero energy bound states with circuit QED in topological insulator junctions
NÚRIA ALCALDE HERRAIZ

Supervisors:
PhD student Ananthu P. Suredran, Quantum Materials and Nanodevices
Prof. Thilo Bauch, Quantum Materials and Nanodevices
Prof. Floriana Lombardi, Quantum Materials and Nanodevices
Examiner:
Prof. Thilo Bauch, Quantum Materials and Nanodevices

Master's Thesis 2023
Department of Microtechnology and Nanoscience (MC2)
Quantum Device Physics Laboratory (QDP)
Chalmers University of Technology
SE-412 96 Gothenburg
Telephone +46 31 772 1000

Cover: The semi-transparent background represents Andreev bound states energy distribution for eight conduction channels with relaxation γ_D and microwave transition γ_{ND} rates indicated by arrows. On solid color there is the scheme of the thesis designed and fabricated device.

Typeset in LaTeX
Printed by Chalmers Reproservice
Gothenburg, Sweden 2023

Towards probing zero energy bound states with circuit QED in topological insulator junctions

NÚRIA ALCALDE HERRAIZ
Department Microtechnology and Nanoscience
Chalmers University of Technology

Abstract

Majorana fermions are aimed to be observed in a spin-non-degenerate system where particle-hole symmetry is imposed. Such a landscape was proposed by Fu and Kane to be formed at the interface between a topological insulator and a superconductor. Topological insulators are insulating materials in the bulk, but that present metallic states with spin non-degeneracy at the surface. These metallic states in the vicinity of an ordinary superconductor become superconducting by proximity effect imposing the particle-hole symmetry, hence an scenario were Majorana fermions observation is possible.
Taking first steps towards Majorana engineering, the aim of the thesis is to study the energy band structure of a STIS junction. The STIS junction studied was made from bismuth selenide nanowires and aluminium electrode contacts and then embedded in a RF-SQUID loop coupled to a resonator. This configuration allowed to characterize the band structure of the STIS junction probing its susceptibility through microwave reflectometry measurements. The experimental data was then compared to an STIS short ballistic junction model obtaining a relaxation parameter $\gamma_D = 2\,\text{GHz}$ and a microwave transitions rate of $\gamma_{ND} = 3\,\text{GHz}$ for probing frequency $4.20\,\text{GHz}$ and $\gamma_{ND} = 10\,\text{GHz}$ at $8.16\,\text{GHz}$.

Keywords: majorana fermions, topological insulator, josephson junction, band structure, susceptibility, microwave reflectometry.

Acknowledgements

I would like to thank my supervisors Thilo Bauch, Floriana Lombardi and Ananthu P. Suredran for their support through this thesis. Thilo, thanks for all the discussion meetings, talking about the ABS, measurement experiments or debugging code and the priority status on the email list. Floriana, thank you for meetings, in your office or zoom, and for your sincerest opinion. And Ananthu, thanks for the clean room hours (not the ones on weekends), your teaching assignments on EBL and for sharing your 'weird ideas'.
Thanks to all the QManD group members: Alexei Kalaboukhov, Riccardo Arpaia, Edoardo Trabaldo, Xavier Palermo, Eric Wahlberg, Kiryl Niherysh, Feike van Veen, Marco Biagi and Andrea d'Alessio. Specially, to Riccardo for your support on corrections and Xavier and Kiryl for those first days following you in the clean room. Also, Feike, Marco, Andrea, 'my desk buddies', I would speak less Italian if not because of you.
I want to give a special mention to the MC2 administrative and technical staff. Particularly, Annika Holtringer for helping me to set in and Mats Hagberg and Henrik Frederiksen for their technical support in the clean room.
Outside Chalmers, there are a few researchers that I would also like to thank. Javier Tejada for starting this a few years ago with a proposed report on Josephson Junctions; Arantxa Fraile Rodriguez for giving me her sincerest opinion and perspective when I panicked upon decisions; PhD Alejandro Hernandez for appointing himself as my scientific mentor; and Teresa Puig to make me want to go back to her group after my Bachelor thesis, even though I am not, thank you.
Without having a direct impact in the thesis realization, I believe I could not have gone through these past few months without the support of my family and friends. Specially, my parents for their unconditional trust and trying to understand what do I study and to my grandparents for discovering video calls because of me. Also, I would like to thank the friends that started as colleagues, as the ones in QT, always trying to drag me to their department, Linus, Ivan and Paul, and the ones that were with me in this master from the beginning Thanos, Saieesh and Awse. Also, I want to thank the friends that understood my 'maybes', 'I can't today' and 'probably next week/month/year'. Gian, Júlia, Pol for those first months that made me an asset in the kitchen; Sabela, Lucía and Lucas for making me arrive to a dinner with 'croquetas' and leaving with a plane ticket to Lithuania; and to the now scattered family from the beginning of this year to make me burst of laugh every time we met. Specially, Montie for your kind words and encouragement (or maybe just for the tiramisù). I could not finish this section without mentioning the friends to whom I said goodbye, but always welcome me when I return Tonis, Geor, Adri, Sara, Neus, Michelle, Helena, Clara, Andrea, Júlia, Laia, Mireia, Marina, Elisa and Azahara. Also, a special thanks to Ruth Haggerty, I hope this thesis makes it up for the never delivered essays, and to Guillem and Gemma for being there since 1997.

Núria Alcalde-Herraiz, Santa Maria de Palautordera, June 2022

List of Acronyms

Below is the list of acronyms that have been used throughout this thesis listed in alphabetical order:

ABS	Andreev Bound State
AC	Alternative Current
AFM	Atomic Force Microscope
BCS	Bardeen Cooper Schrieffer
CPR	Current Phase Relation
CPW	Coplanar Waveguide
DC	Direct Current
EBL	Electron Beam Lithography
JJ	Josephson Junction
N	Normal metal
RF	Radio-frequency
SEM	Scanning Electron Microscope
SC, S	Superconductor
SQUID	Superconducting Quantum Interference Device
TI	Topological Insulator
VNA	Vector Network Analyzer

Nomenclature

Below is the nomenclature of constants, parameters, and variables that have been used throughout this thesis.

Constants

h	Planck constant	$\simeq 6.63 \times 10^{-34} J \cdot s$
$\hbar$	Reduced Planck constant	$= h/2\pi \simeq 1.1 \times 10^{-34} J \cdots$
e	Elementary charge	$\simeq 1.6 \times 10^{-19} C$
k_B	Boltzmann constant	$\simeq 1.38 \times 10^{-23} J/K$
μ_0	Vacuum permeability	$\simeq 4\pi \times 10^{-7} H/m$
Φ_0	Magnetic flux quantum	$= h/2e \simeq 2.07 \times 10^{-15} Tm^2$
f_J	Josephson Frequency	$= 2eV/h \simeq V \times 483.6 MHz/\mu V$

Symbol Definition

φ	Phase difference across a junction
I_C	Critical current
l_{JJ}	Junction length
w_{JJ}	Junction width
t_{JJ}	Junction thickness
T_c	Critical temperature
k_B	Boltzmann constant
h	Planck constant
$\hbar$	Reduced Planck constant
λ_L	London penetration depth
λ_J	Josephson penetration depth
Φ_0	Magnetic flux quantum

e	Elementary charge
μ_0	Vacuum permeability
f_J	Josephson Frequency
L_J	Josephson Inductance
E_J	Josephson Energy
I_S	Screening current
Φ_{ext}	External flux
$\beta_{L,RF}$	Screening parameter
L_k	Kinetic inductance
L_g	Geometric inductance
Δ	Superconducting gap
$\mathbf{T}$	NS transparency
t	Transmission coefficient
c	Nanoribbon circumference cross section
τ_n	Quantized transparency
k_n	Electrons momentum
k_y	Electrons transverse momentum
$f_n^{\pm}$	Fermi occupation probability
χ	Total junction susceptibility
χ_J	Josephson susceptibility
χ_D	Josephson diagonal susceptibility
χ_{ND}	Josephson non-diagonal susceptibility
χ'	Real susceptibility
χ''	Imaginary susceptibility
γ_D	Relaxation rate
γ_{ND}	Microwave transitions rate
w_0, f_0	Fundamental resonator frequency
Q	Resonator quality factor
Q_{int}	Resonator internal quality factor
Q_{ext}	Resonator external quality factor
Γ_r	Reflection coefficient
L_R	Resonator characteristic inductance
C_R	Resonator characteristic capacitance
C_C	Resonator coupling capacitance

L_{SQUID}	SQUID inductance
M	Mutual inductance
L_l	Inductance per unit length
C_l	Capacitance per unit length
R_l	Resistance per unit length
l_{SQUID}	SQUID length
w_{SQUID}	SQUID width
P_c	Circulating power
P_{in}	Input power
N	Number of photons

Contents

List of Figures

List of Tables

1
Introduction

Predicted in 1937 yet still to be observed, Majorana fermions are charge-neural particles that are their own anti-particle. The interest around Majorana fermions arises in their observation per se and the step that represent towards topological quantum computing providing protected error correction [1]. A way to engineer these particles was proposed by Fu and Kane [2] to be formed at the interface between a topological insulator and a superconductor.

Topological insulators (TIs) introduce us to an scenario with an strong spin-orbit coupling, where the magnetic field of the atom nucleus is strongly coupled to the spin of the atom electrons [3]. This relativistic phenomena is reflected in the TIs band structure both in the bulk and at the surface states. In the bulk of the material, the band structure follows an inverted electronic energy band structure with a band-gap like feature as an 'ordinary insulator' [1]. Instead, TIs surface states present a gapless interface state, in other words, a metallic state. And, still influenced by the strong spin-orbit coupling, the electron momentum along the surface remains well defined, and thus the spin of the electron locked [4].

A particularity of these metallic surface states appears when TIs are placed next to Bardeen-Cooper-Schrieffer superconductors, like niobium (Nb) or aluminium (Al), as the metallic state becomes superconducting by proximity effect [5]. Superconductivity brings into the table two constraints: particle-hole symmetry and fermion parity conservation. The former reflecting that interactions between quasi-particles and their anti-particle will be the same and the latter referring that the system will always have an odd or even number of fermions. The confluence between these three properties in the TI-S interface, defined spin, particle-hole symmetry and fermion parity conservation, are the ones making this new interface a landscape predicted to host Majorana fermions. However, when implementing the theorized junction to a fabricated one there are more constrictions, for example to probe Majorana one has to be allocated in the Dirac point of the TI material, which becomes a challenging task to realize. Therefore, the objective of this thesis is to study the energy band structure of a superconductor-topological insulator-superconductor (STIS) junction, taking a first step towards probing Majorana energy states.

We propose the nanofabrication of STIS junctions using bismuth selenide (Bi_2Se_3) nanowires provided by the Institute of Chemical Physics in Latvia University [6] inducing the superconductivity through aluminum electrode contacts. Following recent works [7], [8] we integrated the junction on a superconducting loop and coupled it to a resonator. The aim of this configuration is to probe the susceptibility of the junction through microwave reflectometry measurements. As when the junction is flux biased the susceptibility will present a new adiabatic and dissipation behaviour

that modify the resonator characteristic parameters. When one compares the experimental data of these variations to a short ballistic junction model, one can extract information about the junction energy states.
Overall, this thesis describes the design, fabrication and characterization of STIS junctions. Providing results where one can observe the different mechanisms that drive the band structure of the TI.

The thesis is structured as it follows.

Chapter 2 introduces the macroscopic phenomena in Josephson Junctions, and describes the mesoscopic transport of the junctions first through a superconducting-normal metal-superconducting junction and afterwards through a superconducting-topological insulator-superconducting junction. Also, a probing set-up for the STIS junctions is given. Chapter 3 describes the devices design, nanofabrication and characterization. Measurement results are showed and discussed in Chapter 6. Chapter 7 is devoted to conclusions and future outlook.

2

Theory

Majorana fermions are aimed to be engineered placing a superconductor on the surface of a topological insulator. In other words, weakly coupling two superconductor electrodes through a TI. This junction receives the name of Josephson Junction (JJ) and conventionally an insulator or a normal metal is used to couple the two superconductor electrodes.

Therefore, before focusing on our particular case, conventional JJs are briefly defined through a macroscopic point of view. The transition from a conventional weak link to a TI is done while discussing the mesoscopic transport in the junctions. Because using TI weak links enable to discuss Majorana bound states, this chapter concludes with a proposed probing setup.

2.1 Macroscopic treatment of Josephson Junctions

This first section introduces the Josephson equations, the concept of Josephson inductance and the use of Josephson Junctions as magnetosensors.

2.1.1 AC and DC Josephson Equations

Josephson Junctions are formed by two superconducting electrodes weakly coupled through a barrier. Conventionally, the barrier, named weak link, can be made from either a geometrical constriction or a different material such as an insulator, a semiconductor, a normal metal or another superconductor with lower critical temperature, T_C, than the electrodes. In 1962 it was predicted that for very thin barriers, Cooper pairs can tunnel from one superconductor electrode to the other without any applied voltage [9]. The phenomena received the name of the Josephson Effect and was proven a year later [10].

The Josephson Effect can be described through a microscopic viewpoint using the Bardeen-Cooper-Schrieffer (BCS) theory. According to BCS theory, the Cooper pairs in each superconducting electrode are in the same quantum state, thus they can be described by a single wavefunction, $\Psi(\theta) = |\Psi^0| \exp i\theta$. Here, the amplitude reflects on a local density of Cooper pairs and the phase on the superconducting order parameter of each electrode. Because inside a JJ the two superconductor electrodes are weakly coupled, their wavefunctions overlap inside the barrier and enable the tunneling of Cooper pairs, see Figure 2.1. The dissipationless tunneling current is related with the superconducting critical current of the electrodes and the

phase difference between the two electrodes $\varphi = \theta_R - \theta_L$ by:

$$I = I_c \cdot \sin\varphi \tag{2.1}$$

This equation is known as *DC Josephson Effect* and it is used to describe the current-phase relation (CPR) of ordinary JJs. However, Josephson introduced a second equation to describe the Josephson Effect[9].

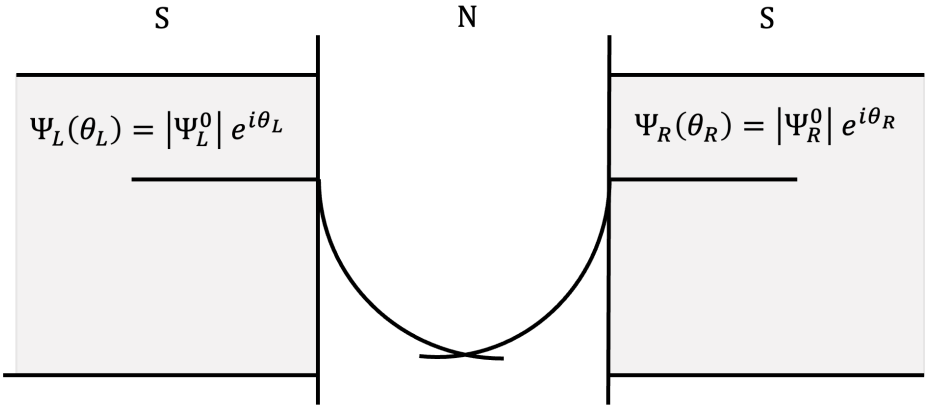

Figure 2.1: Schematic of a Josephson Junction. Indicated there is the wavefunction of the two superconductors and their overlap inside the weak link that enables de Josephson Current.

The second equation, *AC Josephson Effect*, describes the behaviour of JJs when a potential difference is applied. In this scenario the phase difference of the junction changes over the barrier according to:

$$V = \frac{\hbar}{2e}\frac{\partial\varphi}{\partial t} \tag{2.2}$$

where $\hbar$ is the reduced Plank constant and e is the electron charge. Equation (2.2) allows to obtain the phase difference as a function of time and the Josephson frequency:

$$f_J = \frac{\omega_J}{2\pi} = \frac{2eV}{h} = \frac{V}{\Phi_0} = V \cdot 484MHz \tag{2.3}$$

Here, Φ_0 is the quantum flux and can be related to the Planck constant h and the electron charge e by $2e/h = 1/\Phi_0$. As equation (2.3) relates frequency and voltage through fundamental constants JJs can be used as a voltage standard.

2.1.2 Josephson Inductance

When the junction phase varies over time, it reflects both on the voltage across the junction, equation (2.2), and the current, equation (2.1). Hence, both equations can be used to understand the dynamics of JJs.
By differentiating equation (2.1) and replacing $\frac{\delta I}{\delta t}$ in equation (2.2), one obtains:

$$V = \frac{\hbar}{2eI_C\cos\varphi}\frac{\partial I}{\partial t} = L_J\frac{\partial I}{\partial t} \tag{2.4}$$

which is an expression that reflects on a non-linear inductance behaviour of JJs where

$$L_J = \frac{\hbar}{2eI_C \cos\varphi} = \frac{\Phi_0}{2\pi I_C \cos\varphi} \tag{2.5}$$

is called Josephson inductance. At this point, it is interesting to calculate the energy stored inside the junction:

$$E_J = \int_0^t I \cdot V dt = \frac{\Phi_0}{2\pi} I_c (1 - \cos\varphi) \tag{2.6}$$

where I has been substituted by *DC Josephson Effect* expression, equation (2.1), and V by *AC Josephson Effect*, equation (2.2). The non-linear potential obtained has been exploited in quantum computation field as the non-harmonicity allows to emulate two-level systems [11].
The energy expression of equation 2.6 allows to derive a new CPR of the Josephson Junction:

$$I(\varphi) = \frac{2\pi}{\Phi_0} \frac{\partial E_J}{\partial \varphi} \tag{2.7}$$

And through it a generalized Josephson inductance:

$$\frac{1}{L} = \left(\frac{2\pi}{\Phi_0}\right)^2 \frac{\partial^2 E_J}{\partial \varphi^2} \tag{2.8}$$

These last two equations will be relevant in the following sections, when Josephson Junctions are evaluated using a TI as a weak link and not a conventional barrier.

2.1.3 Superconducting Quantum Interference Devices (SQUIDs)

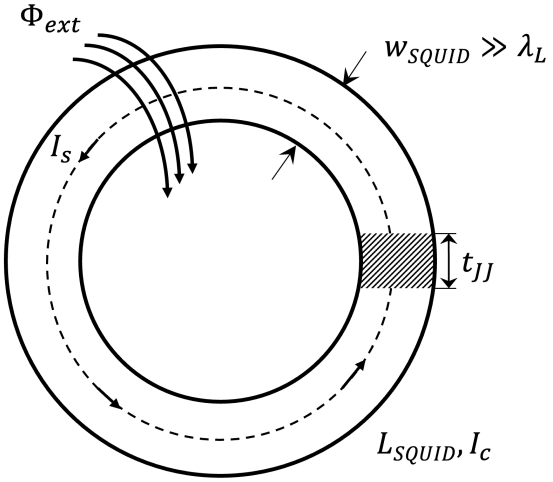

Figure 2.2: Schematic representation of a RF-SQUID: a superconducting loop with inductance L_{SQUID} and width $w_{SQUID} \gg \lambda_L$ and critical current I_C interrupted by a weak link of thickness t_{JJ}. The external flux Φ_{ext} and the screening current I_S in response are also indicated.

One of the conventional applications of JJs are Superconducting Quantum Interference Devices (SQUIDs). SQUIDs are highly sensitive magnetosensors that consist of

a superconducting loop of inductance L_{SQUID} interrupted by one (RF) or two (DC) parallel Josephson junctions. The device is able to operate combining the phenomena of fluxoid quantization and Josephson effect. Focusing on the RF-SQUID, to understand its operation the variation of the screening current as a function of the magnetic flux, and vice versa, needs to be derived. From the fluxoid quantixation in a superconducting loop, we obtain:

$$\varphi = 2\pi(n - \Phi/\Phi_0) \tag{2.9}$$

where Φ_0 is the flux quantum and Φ is the total magnetic flux inside the loop which is the sum of the external flux Φ_{ext} and the self-induced flux created by the loop screening current I_S:

$$\Phi = \Phi_{ext} + I_s L_{SQUID} \tag{2.10}$$

Inserting equation (2.9) in equation (2.1), the *DC Josephson effect*:

$$I_s = -I_c \sin\left(2\pi\frac{\Phi}{\Phi_0} + \beta_{L,RF}\frac{I_s}{I_0}\right) \tag{2.11}$$

where we introduce the screening parameter $\beta_{L,RF} = 2\pi I_c L_{SQUID}/\Phi_0$. This parameter is key to study the effect of loop inductance in the response of the SQUIDs critical current as a function of an external applied magnetic flux. Equivalently, the flux across the junction can be deduced:

$$\Phi = \Phi_{ext} - \frac{\Phi_0}{2\pi}\beta_{L,RF} \sin\left(2\pi\frac{\Phi_{ext}}{\Phi_0} + \beta_{L,RF}\frac{I_s}{I_0}\right) \tag{2.12}$$

Equations (2.11) and (2.12) describe the physics of the RF-SQUID and have to be solved numerically. However, a qualitative analysis of the RF-SQUID operation can be done considering the screening parameter $\beta_{L,RF}$. In the presence of an external field, when $\beta_{L,RF} \ll 1$, the self-induced flux due to the screening contribution becomes negligible and the total flux across the RF-SQUID is proportional to the external flux applied. Instead, when $\beta_{L,RF} >1$, equation 2.12 becomes multivalued. As it can be seen in Figure 2.3 the flux behaviour becomes sinusoidal-like with increasing amplitude as $\beta_{L,RF}$ increases. However, when $\beta_{L,RF}$ is high enough, $\beta_{L,RF} = 10$ in the figure, the physical behaviour differs from the mathematical one as the screening current tries to oppose Φ_{ext}, until the critical current of the loop is reached. Then, the RF-SQUID becomes resistive, and one flux quantum is allowed inside the loop until superconductivity is restored. This hysteric behaviour is reflected in Figure 2.3 by arrow jumps.

As a final note, it is important to consider that the SQUID inductance L_{SQUID} has two components: the geometric inductance $L_g \approx \mu l_{JJ}$ (again, l_{JJ} is the junction length), and the kinetic inductance $L_k = \mu_0\lambda_L^2/wt$ (where λ_L is the London penetration depth, and w and t are the width and the thickness of the superconducting electrodes).The kinetic inductance L_k is related to the kinetic energy of the circulating current, in other words, to the inertial mass of the Cooper pairs under an alternating electric field. Therefore, L_k is a parameter related to the density of Cooper pairs and thus to the temperature T. Hence, L_k decreases as the Cooper pair density increases and T decreases. Furthermore, L_k is dominant when the

width w_{SQUID} and/or the thickness t_{SQUID} of the SQUID loop are comparable to or smaller than the London penetration depth λ_L.

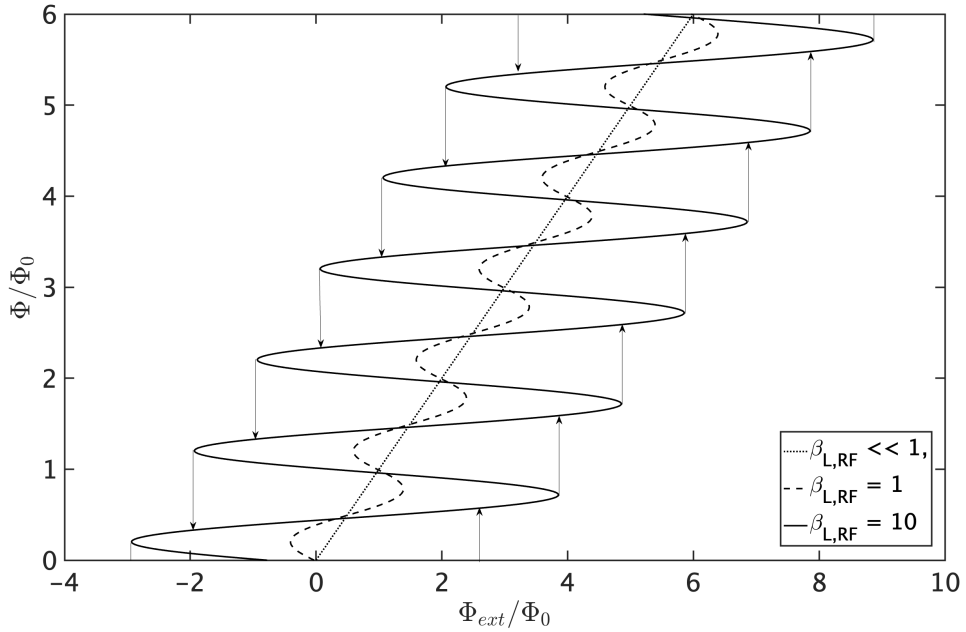

Figure 2.3: Normalized total flux Φ/Φ_0 as a function of the normalized external flux Φ_{ext}/Φ_0.

2.2 Microscopic treatment of a Josephson Junction

Topological insulators hold metallic surface states, therefore, analogously when a metal (N) is in the vicinity of a BCS superconductor (SC), Cooper pairs can leak from the superconductor to the surface modifying its properties. This is the so-called proximity effect and despite being first discussed by Gennes [5], the transport mechanism underneath was proposed by Andreev [12].
To understand the mesoscopic transport for a Josephson Junction with a TI weak link, it is important to first describe the transport phenomena within a superconductor-normal metal-superconductor (SNS) junction and then to apply the constrictions born from using a TI, as its metal surface states are key for the transport.

2.2.1 Superconductor-normal-superconductor junction

A SNS junction presents two media, the normal metal and the superconductor, where the current is transported by single electrons, for the former, and by Cooper pairs, for the later. To enable the transport through the junction there has to be a mechanism that enables the Cooper pairs to turn into electrons and single electrons to combine in Cooper pairs. As stated beforehand, the transport mechanism was described by Andreev [12] and is schematized in Figure 2.4. As it is illustrated, Andreev proposed that an electron with $E < \Delta$ traveling within the N region can couple with one of the Fermi sea of the normal metal, hence both can be transferred

as a Cooper pair. Moreover, to preserve charge and momentum, a hole is formed in the normal metal with energy $-E$. This process is also reversible, if a hole approaches the NS interface a Cooper pair will be annihilated and an electron back-scattered. Overall, the mechanism is called Andreev reflection and is described as an elastic scattering phenomena where the total energy and spin are conserved. In the SNS junction it leads to the formation of a bound state called Andreev Bound States (ABS).

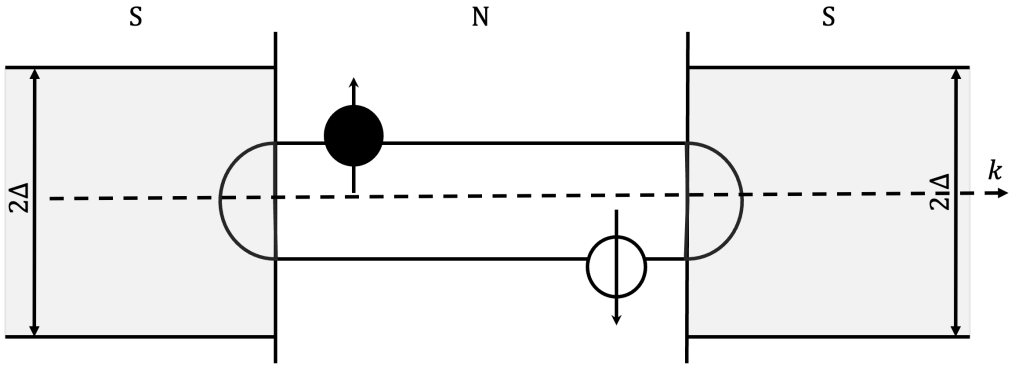

Figure 2.4: Schematic representation of an ABS in the normal metal region of an SNS junction.

From this point on-wards, the mesoscopic transport considerations will be for a short ballistic junction, where the conduction channel with length l is shorter than the superconducting coherence length ξ_N. Particularly, the one dimensional case. According to reference [13], the energy dependence of ABS with respect the phase difference across the junction φ is a periodic function given by

$$E^{\pm}(\varphi) = \pm\Delta\sqrt{1 - \mathcal{T}\sin^2\varphi/2} \tag{2.13}$$

where the $\pm$ sign refers the upper and lower energy bands and $\mathcal{T}$ to the transparency of the junction. If we plot the energy expression, Figure 2.5, it can be appreciated that the value of the gap between two Andreev bound states at $\varphi = \pi$ depends on the transparency at the interface $\mathcal{T}$.

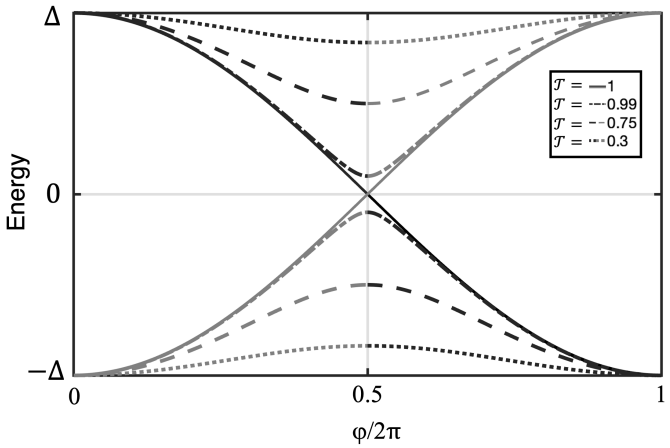

Figure 2.5: ABS for junction transparencies $\mathcal{T} = 1, 0.99, 0.75$ and 0.30.

The transparency of the junction is also related to the transmission probability as $\mathcal{T} = |t|^2$ [14], therefore, for a normal metal weak link there is still a probability that a travelling electron does not combine with an electron of the Fermi sea to be transmitted to the superconductor. In other words, the electron can be backscattered at the NS interface. This scenario, where the electron is backscattered instead of transmitted is the most feasible due to material limitations in SNS junctions.

2.2.2 Superconductor-topological insulator-superconductor junction

Here is when to consider the STIS is interesting as TIs are materials that present strong spin-orbit coupling [1], [15]. This relativistic interaction describes the coupling between the magnetic field generated by an atom nucleus and an electron circulating around it. The coupling depends on both the direction and magnitude of the electron as well as its spin-orientation. As a consequence, when the coupling occurs the electron spin locks. If this electron faces the TI-S interface it can not backscatter as an electron, as it will imply changing the spin orientation. This is the scenario were Andreev Bound States are depicted as Majorana bound states. In other words, to look for Majorana, is to look for a protected zero energy crossing that reflects on $\mathcal{T} = 1$ or transmission $t = 1$.

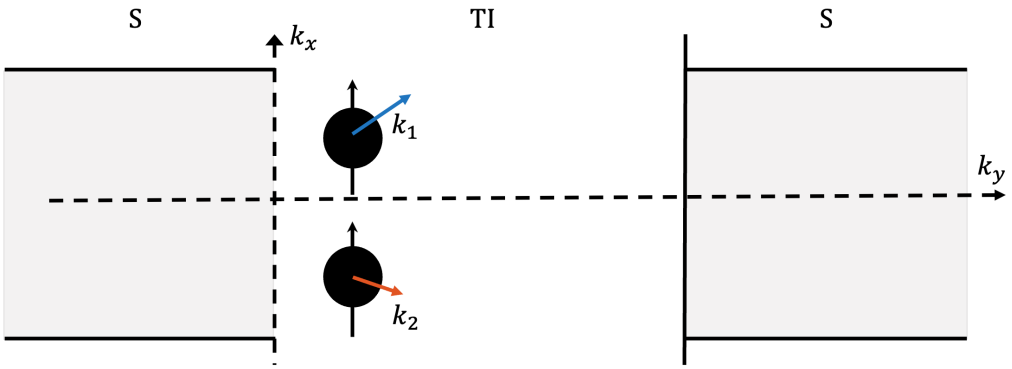

Figure 2.6: Schematic representation of electrons with electron momentum k_n for $n = 1, 2$ in the topological insulator region of an STIS junction with finite width.

However, when we extend the formalism to a junction with a finite width, this protected backscattering breaks down because the electrons trajectories follow a finite angle [16]. As a consequence, the energy spectrum is redefined, turning equation (2.13) to

$$E_n^{\pm}(\varphi) = \pm\Delta\sqrt{1 - \tau_l \sin^2 \varphi/2} \tag{2.14}$$

where each transparency has associated a quantized vector k_n corresponding to the electron momentum [14]. This is schematized in Figure 2.6. Therefore, every single pair of ABS is defined by a conduction channel and the overall consideration of the channels establishes the superconducting current inside the weak link.
For the particular case of TI nanoribbons with a circumference cross section $c = 2w_{JJ}+2t_{JJ}$ being w_{JJ} the width and t_{JJ} the nanoribbon thickness, the transparency

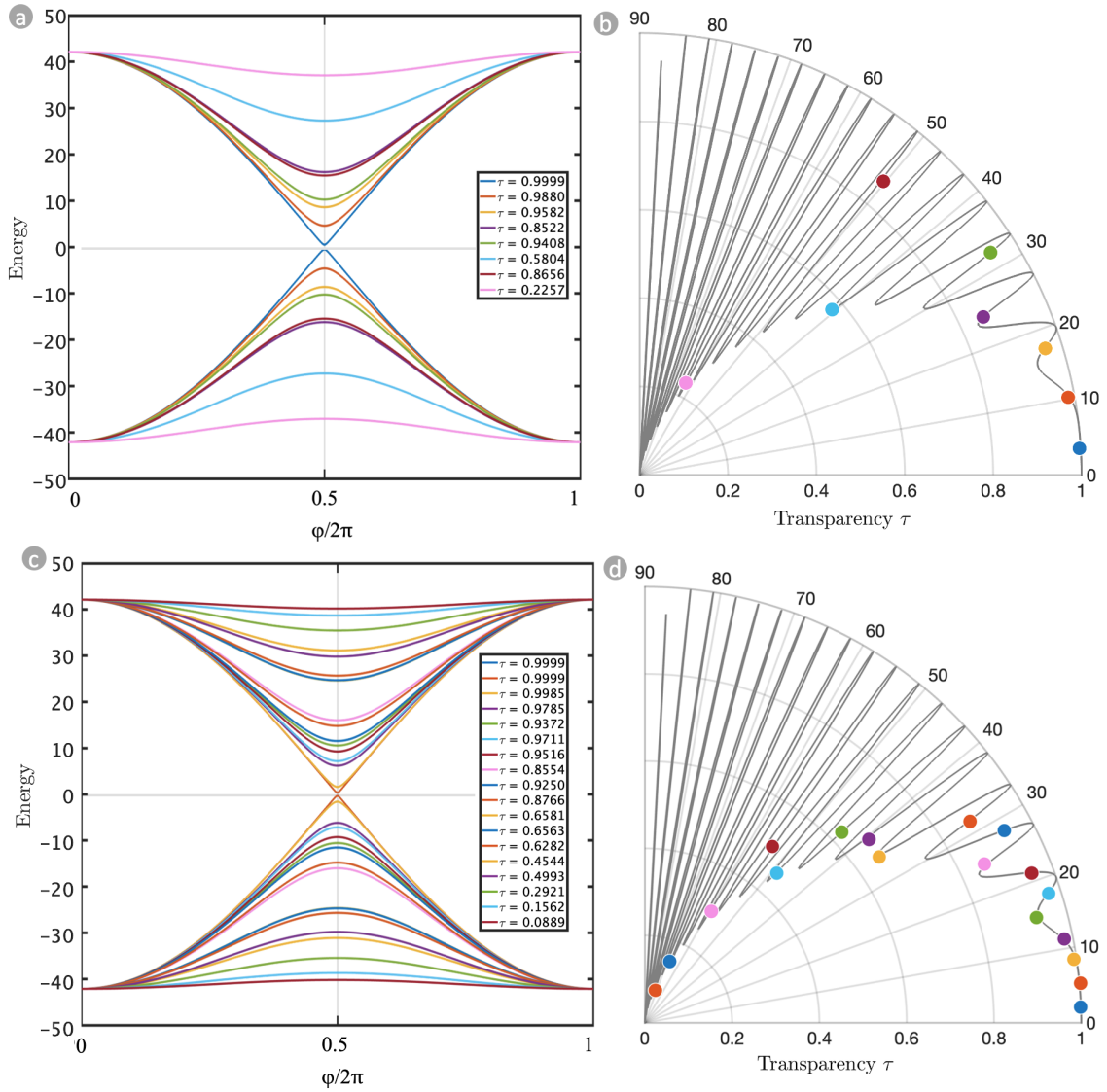

Figure 2.7: A comparison about the geometry impact on ABS : (a) Energy dispersion for a junction of thickness $t_{JJ} = 19\,\text{nm}$ and $w_{JJ} = 25\,\text{nm}$. (b) Transparency against the angle between the propagation direction and the normal to the interfaces for a junction of thickness $t = 19\,\text{nm}$ and $w_{JJ} = 25\,\text{nm}$. (c) Energy dispersion for a junction of thickness $t_{JJ} = 19\,\text{nm}$ and $w_{JJ} = 75\,\text{nm}$.(d) Transparency against the angle between the propagation direction and the normal to the interfaces for a junction of thickness $t_{JJ} = 19\,\text{nm}$ and $w_{JJ} = 75\,\text{nm}$.

τ quantization relies on transverse momentum k_y perpendicular to the current [17], being

$$\tau_n = \frac{k_n^2}{k_n^2 \cos k_n L + (\mu/\hbar v_f)^2 \sin^2 k_n L} \tag{2.15}$$

where the electron momentum $k_n = \sqrt{(\mu/(\hbar v_f))^2 - k_y^2}$ and transverse electron momentum $k_y = (n + \frac{1}{2})\frac{2\pi}{c}$ with integer $n = 0, 1, 2, ...$ [18]. Therefore, it is interesting to analyse the energy spectrum of a short STIS junction as a function of c. This is illustrated in Figure 2.7 that depicts the ABS of junctions of thickness $t_{JJ} = 19\,\text{nm}$ and width $w_{JJ} = 25\,\text{nm}$ in Figure 2.7(a), and $w_{JJ} = 75\,\text{nm}$ in Figure 2.7(c). When these two figures are compared, it is clearly seen that the number of channels increases

when c does. The figure also shows the τ of the junctions against the angle between the propagation direction and the normal to the interfaces $\theta = \arctan k_y/k_n$ for a continuous -line- and quantized -dots- case. Analogously Figure 2.7(b) corresponds to the junction of width 25 nm and Figure 2.7(d) to junction $w_{JJ} = 75\,\text{nm}$. Note that for Figure 2.7(c) $\tau = 0.9999$ is repeated, however when compared to Figure 2.7(d) the trajectories vary, this is due to lack of numeric resolution in the graph.
As stated before, the overall consideration of each conduction channel, each ABS single pair, establishes the superconducting current inside the weak link. In fact, the CPR can be found inserting the energy spectrum of equation (2.14) in equation (2.7):

$$I(\varphi) = -\frac{e\Delta}{2\hbar}\sum_n \frac{\tau_n \sin\varphi}{\sqrt{1-\tau_n \sin^2\varphi/2}} \tag{2.16}$$

When the temperature considered is different from zero, $T \neq 0$, the energy populations will vary according to Fermi-Dirac statistics, turning the CPR to:

$$I(\varphi) = \frac{2e}{\hbar}\sum_n \frac{\partial E_n^+(\varphi)}{\partial\varphi} f_n^+ + \frac{\partial E_n^-(\varphi)}{\partial\varphi} f_n^- \tag{2.17}$$

where a f_n^+ and f_n^- are the Fermi occupation probabilities of the two levels corresponding to $f_n^\pm = 1/(1+\exp(E(\varphi)/k_B T))$. That can be simplified as:

$$I(\varphi) = \frac{2\pi\Delta^2}{4\Phi_0}\sum_n \frac{\tau_n \sin\varphi}{(E_n^+(\varphi))^2}\cdot\tanh(\frac{E_n^+(\varphi)}{2k_B T}) \tag{2.18}$$

Until this point the energy spectrum of a STIS has been described with an emphasis on the impact of the junctions dimensions on the ABS conformation. Furthermore it has been stated that the superconducting current depends on the contributions of each conduction channel. The step that follows is to define an observable that reflects on this energy spectrum.

2.2.3 The TI Susceptibility

As hinted in the title of this section, an observable that reflects on the energy spectrum is the TI susceptibility χ. This observable is not as foreign as it may seem if we go back to Section 2.1.2 which models JJs as non-linear inductances L. Section 2.1.2 concludes giving a generalized inductance expression in equation (2.8) which relates the inverse of the inductance $1/L$ with the second derivative of the junction's stored energy $\delta^2 E_J/\delta\varphi^2$. Now, if one considers that χ is proportional to the inverse of the inductance $\chi = 1/L$, one can turn equation (2.8) to

$$\chi_J = \left(\frac{2\pi}{\Phi_0}\right)^2 \frac{\partial^2 E_J}{\partial\varphi^2} \tag{2.19}$$

Moreover, through equation (2.7) one can relate the JJ current I and the energy first derivative $\delta E_J/\delta\varphi$, so equation (2.19) becomes:

$$\chi_J = \frac{2\pi}{\Phi_0}\frac{\partial I(\varphi)}{\partial\varphi} \tag{2.20}$$

Equation (2.20) relates the junctions susceptibility and the Josephson current which reflects on the ABS as described in the last section. This susceptibility term is referred in literature as *Josephson Susceptibility* χ_J [7], [19] and is purely adiabatic. However, when the junction is AC biased with a certain probing frequency ω, two new non-adiabatic susceptibility contributions arise. One term that reflects on population relaxation of the Andreev levels with a relaxation rate γ_D:

$$\chi_D(\omega) = -\sum_n i_n^2 \frac{\partial f_n}{\partial \epsilon_n} \frac{i\omega}{\gamma_D - i\omega} \tag{2.21}$$

where i_n is the phase dependent current of bound state n and $\frac{\partial f_n}{\partial \epsilon_n}$ is the derivative of this Andreev level occupation. This non-adiabatic relaxation term receives the name of *Diagonal Susceptibility*, as the current i_n can be derived from the diagonal terms of the current operator for Bogoliubov–de Gennes Hamiltonian of a short ballistic SNS junction.

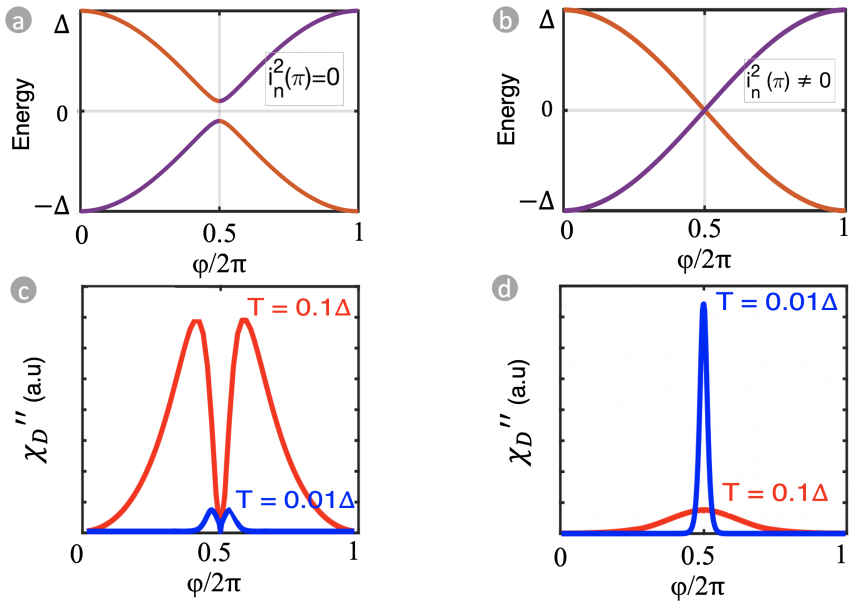

Figure 2.8: (a) A single pair of ABS for transparency different than one ($\tau \neq 1$). (b) A single pair of ABS for transparency one ($\tau = 1$). (c) Imaginary component of the Diagonal Susceptibility for a channel of ($\tau \neq 1$). The $i_n(\pi) = 0$ leads to a characteristic two-peak behaviour. (d) Imaginary component of the Diagonal Susceptibility for a channel of $\tau = 1$. The $i_n(\pi) \neq 0$ leads to a characteristic single-peak behaviour. Figures (c) and (d) are from [20].

Moreover, as i_n is proportional to the phase derivative of the ABS energy, $i_n \propto \partial E_n^+/\partial\varphi$, the behaviour of χ_D is interesting to analyse, particularly its imaginary component χ_D''. This is because its genuine reflection of the TI band structure, which can be seen in Figure 2.8. Here two scenarios are proposed: a junction with a conduction channel of transparency different than one ($\tau \neq 1$), Figure 2.8(a), and a junction with a conduction channel of transparency equal to one ($\tau = 1$), Figure 2.8(b). Because of $i_n \propto \partial E_n^+/\partial\varphi$, when the energy levels do not cross, χ_D'' translates into a two-peak dissipative response at $\varphi = \pi$, Figure 2.8(c). Instead, when the energy levels cross χ_D'' presents a single-peaked behaviour, Figure 2.8(d). However, when considering a junction with finite width, there is going to be more

than one conduction channel, in other words more than one single pair of ABS to be considered.
Let's not forget that there was another susceptibility term arising from ac-biasing a JJ: the *Non-diagonal Susceptibility*. This second term derives from the induced microwave transitions within the Andreev spectrum and it receives its name after the non-diagonal term of the current operator for Bogoliubov–de Gennes Hamiltonian of a ballistic SNS junction.

$$\chi_{ND}(\omega) = -\sum_{n,m\neq n} |i_{nm}|^2 \frac{f_n - f_m}{\epsilon_n - \epsilon_m} \frac{i\hbar\omega}{i(\epsilon_n - \epsilon_m) - i\hbar\omega + \hbar\gamma_{ND}} \tag{2.22}$$

where γ_{ND} is the non-diagonal relaxation term and it presents a single-peak behaviour at $\varphi = \pi$ when γ_{ND} is similar or larger than the probe frequency ω.
Overall, the total ac-susceptibility response for a STIS junction can be defined as

$$\chi(\omega) = \chi_J - \chi_D - \chi_{ND} \tag{2.23}$$

Hence, when probing the susceptibility of an ac-biased junction one obtains:

$$\chi(\omega) = \chi'(\omega) + i\chi''(\omega) \tag{2.24}$$

In contrast with a unbiased junction, where the susceptibility χ is equivalent to the *Josephson Susceptibility* χ_J and is purely real. Therefore, the two new susceptibility terms, χ_D and χ_{ND}, contribute to the real $\chi_{'}$, in addition to χ_J, and the imaginary susceptibility component $\chi_{''}$. Furthermore, these two mechanisms are frequency dependent, so its contributions to the susceptibility vary with the probing frequency. We expect that they follow the behaviour described in reference [20]. In particular for the dissipative component they propose that at low frequency, χ'' is dominated by χ_D, whereas at high frequency the term that dominates the dissipative response is χ_{ND}. In Section 2.2.4 we proposed a measuring set-up to analyse this response and characterize the band structure.

2.2.3.1 The TI: Bismuth Selenide

The TI material used in this thesis is bismuth selenide (Bi_2Se_3) which is an archetypical tetradymite. Tetradymites are M_2X_3 compounds, where M is a group V metal and X is a group VI anion, that crystallize in a rhombohedral structure. As seen in Figure 2.9, the unit cell of Bi_2Se_3 is build by a five layers stacked along z-direction. Referred as quintuple layer the coupling within is stronger between two quintuple layers, being this of the Van der Waals type [1], [15].
In the bulk, Bi_2Se_3 presents an inverted band structure as consequence of the strong spin orbit coupling of the elements. However, the metallic surface states were theorized and supported by angular-resolved photoemission spectroscopy to consist of a single Dirac cone [4].

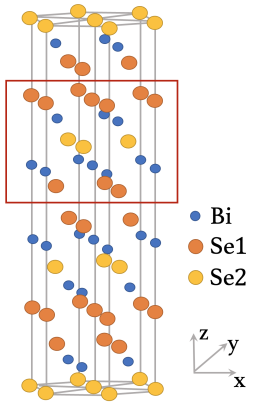

Figure 2.9: Crystal structure of Bi_2Se_3 with a quintuple layer marked in red.

2.2.4 Probing the Josephson Susceptibility

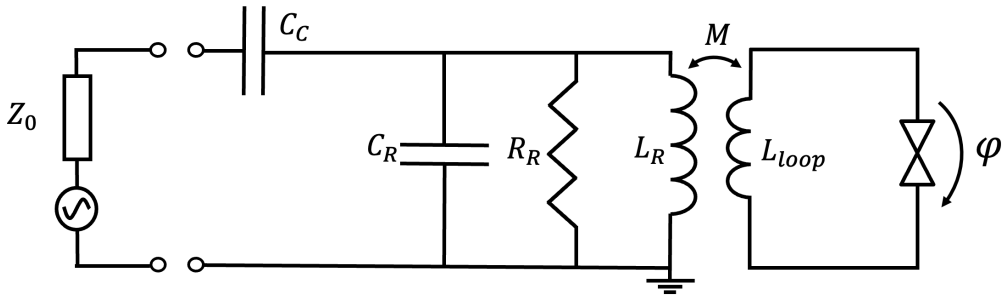

Figure 2.10: Circuit schematic of a RF-SQUID coupled to a $\lambda/4$ resonator. The RF-SQUID has a loop impedance L_{loop} connected in parallel with a JJ that is flux biased. The RF-SQUID couples inductively to the $\lambda/4$ resonator with strength M. The $\lambda/4$ resonator can be modelled as lumped inductance L_R, lumped resistance R_R and lumped capacitance C_R and couples capacitively C_C to the reflectometry setup.

In recent works [7], [19]–[21] susceptibility measurements of STIS junctions have been carried embedding the junction in a RF-SQUID and applying an ac phase-bias φ to it. To probe the susceptibility, the RF-SQUID is coupled to a multimode superconducting resonator.
Throughout this thesis, we have used quarter wavelength resonators, realized by a coplanar waveguide (CPW) transmission line of length $l = \lambda/4$. The effective circuit around the resonance frequency of $\lambda/4$ resonator circuit can be seen in Figure 2.10 as a parallel of a lumped inductance L_R, lumped capacitance C_R and lumped resistance R_R, and a coupling capacitance C_C through which the resonator is probed to perform microwave reflectometry measurements. Through these measurements, one obtains the reflection coefficient Γ_r which reflects on the variation of the input and output circuit signal [22], [23].
Note that the effective circuit of the resonator is derived from the equivalent distributed element circuit around the resonance frequency relating the lumped elements to their equivalent per unit length, using $L_R = 8L_l l/\pi^2$ for the inductance, $C_R = C_l \cdot l/2$ for the capacitance and $R_R = Z_0/\alpha l$ for the resistance where Z_0 is the characteristic impedance $Z_0 = \sqrt{L_l/C_l}$ and α reflects on the real part of the propagation constant of the signal in the transmission line.
There are two key parameters to characterize the resonator: the fundamental resonance frequency ω_0 and the quality factor Q. And both will be modified when the resonator couples to a RF-SQUID. In the following sections ω_0 and Q are going to be defined and then their variation quantified and related to χ.

2.2.4.1 Parameters that describe a $\lambda/4$ resonator, ω_0 and Q

The fundamental resonance frequency ω_0 of the resonator can be defined as:

$$\omega_0 = \frac{1}{\sqrt{L_R C}} \tag{2.25}$$

where L_R is the lumped inductance of the resonator and C the sum of the lumped capacitance C_R and the coupling capacitance C_C. Out of ω_0 one can extract the

multiple harmonics of the resonator as they are odd multiples of the resonators length $l = n\lambda/4$, being $w_n = nw_0$ with $n = 1, 3, 5, 7....$
The quality factor Q is defined by the ratio of energy stored in the resonator to the energy loss per cycle times. It distinguishes between internal Q_{int} and external or coupling Q_{ext} losses, being Q defined by the parallel of the two terms:

$$Q = (\frac{1}{Q_{int}} + \frac{1}{Q_{ext}})^{-1} \tag{2.26}$$

2.2.4.2 Variation of the parameters that describe a $\lambda/4$ resonator, $\frac{\delta\omega}{\omega_0}$ and $\delta\frac{1}{Q}$

As advanced, when the resonator couples to the RF-SQUID, Figure 2.10, both ω_0 and Q vary. To define such variation it is important to define the contribution of the RF-SQUID. In our device the $\lambda/4$ CPW resonator is inductively coupled to a RF-SQUID, the strength of the coupling is represented by the mutual inductance, M. Also, the RF-SQUID is modeled as a loop with self-inductance L_{loop} in parallel with a JJ with inductance L_{JJ}, this last term is the one equal to the inverse of the susceptibility $L_{JJ} = 1/\chi$. Therefore, the RF-SQUID inductance is the sum of the two terms $L_{SQUID} = L_{loop} + 1/\chi$. Thus, the total inductance to consider in equation (2.26) is:

$$L = L_R - \frac{M^2}{L_{SQUID}} \tag{2.27}$$

And the resonance frequency in equation (2.26) becomes:

$$\omega = \frac{1}{\sqrt{(L_R - \frac{M^2}{L_{SQUID}})C}} \tag{2.28}$$

Using the Taylor expansion on equation (2.28), one obtains that the resonance frequency variation $\delta\omega = \omega - \omega_0$ is:

$$\frac{\delta\omega}{\omega_0} = \frac{1}{2}\frac{M^2}{L_R}\frac{1}{L_{SQUID}} \tag{2.29}$$

where it has been argued [7], [20] that the term $\frac{1}{L_{SQUID}}$ reflects on the susceptibility χ. Particularly, it can correlated with the real χ' susceptibility component as:

$$\frac{\delta\omega}{\omega_0} = \frac{1}{2}\frac{M^2}{L_R}\chi' \tag{2.30}$$

The quality factor is related to the relative frequency variation as $Q = f_0/\delta f$ [22] and it is proposed that Q relates to the imaginary component of the susceptibility χ'':

$$\delta\frac{1}{Q} = \frac{1}{2}\frac{M^2}{L_{SQUID}}\chi'' \tag{2.31}$$

Note, the resonance shift can also be obtained following R.Halle derivation from [8]. In his work he determines the frequency variation considering the influence of a

purely inductive Z_{load} coupled to the $\lambda/4$ resonator, the result is as follows

$$\frac{\delta f}{f_0} = \frac{8}{\pi^2}\frac{M^2}{L_R}\chi' \tag{2.32}$$

where one can relate $w = 2\pi f$. As it can be seen there is a $8/\pi^2$ prefactor that mismatches equation 2.31. Moreover, in some works [7], [19], [20] the 1/2 factor on equation (2.31) is disregarded, but in this thesis, out of definition, it has been maintained here as it does not interfere with the result discussion.

3

Methods

The following chapter focuses on translating Figure 2.10 onto a physical devices and its characterization. The first section contemplates design details of the patterned resonator and RF-SQUID, followed by the nanofabrication process and the experimental set-up and fittings used to characterize the device.

3.1 Devices Design

The overall design consisted on two $\lambda/4$ CPW resonators, Figure 3.1a, and the corresponding RF-SQUIDs patterned on a 5 mm $\times$ 5 mm chip, Figure 3.1b with a junction close up in Figure 3.1c. The following section focuses on giving the specifications of the $\lambda/4$ resonators and the RF-SQUIDs.

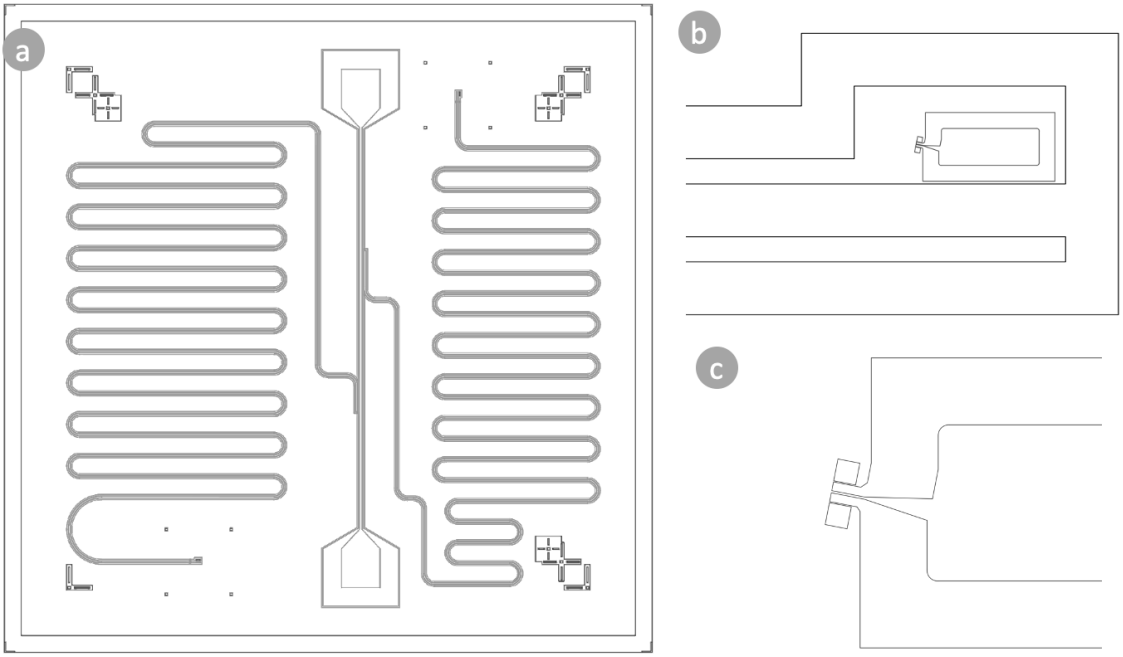

Figure 3.1: Devices design. (a) Overall CAD design of chip, the two $\lambda/4$ CPW resonators can be seen on each side of the chip. (b) Close-up of the RF-SQUIDS coupled to the $\lambda/4$ CPW left resonator. (c) Close-up to the RF-SQUID junction.

3.1.1 $\lambda/4$ CPW Resonators

Two $\lambda/4$ CPW resonators were patterned on a 100 nm thin NbN films on a 525 µm thickness sapphire substrate with lengths $l^L_{\lambda/4} = 36\,\text{mm}$ and $l^R_{\lambda/4} = 30\,\text{mm}$, where the super-index, R or L, corresponds to the position on the chip, left or right. The characteristic parameters of the resonator were obtained via a Matlab software and the final design simulated in Sonnet. As seen in Table 3.1, the two resonators were chosen to have the same inductance L_l, resistance R_l and capacitance C_l per unit length. However, the coupling capacitance C_C was also modified for each resonator. The result were two $\lambda/4$ CPW resonators with fundamental frequencies at 872 MHz and 1.05 GHz.

Component		Resonator $l^L_{\lambda/4} = 36\,\text{mm}$	Resonator $l^R_{\lambda/4} = 30\,\text{mm}$
Inductance per unit length	L_l	0.41 µH/m	0.41 µH/m
Resistance per unit length	R_l	10 µΩ/m	10 µΩ/m
Capacitance per unit length	C_l	157 pF/m	157 pF/m
Couple capacitance	C_C	28 fF	70 fF
Fundamental frequency	f_0	872 MHz	1.05 GHz

Table 3.1: Specifications on the $\frac{\lambda}{4}$ NbN Resonators.

The design of the resonators was done taking into account a measuring band-pass between 4 GHz and 8 GHz. Thus, the fundamental frequency was picked to enable different harmonics to fall into that band-pass. However, after fabrication there was a shift on the fundamental frequencies of both resonators. Particularly, the $l = 36$ mm resonator moved from 872 MHz to 628 MHz and the $l = 30$ mm resonator moved from 1.05 GHz to 720 MHz. We attribute this change to a variation of the kinetic inductance of the NbN thin film, however more exploration is required. The final harmonics to fall into the band-pass are given in Table 3.2.

Harmonic n	Resonator $l^L_{\lambda/4} = 36\,\text{mm}$	Harmonic n	Resonator $l^R_{\lambda/4} = 30\,\text{mm}$
7	4.40 GHz	5	3.70 GHz
9	5.65 GHz	7	5.29 GHz
11	6.91 GHz	9	6.80 GHz
13	8.16 GHz	11	8.30 GHz

Table 3.2: Harmonics within the 4 GHz and 8 GHz band-pass of the nanofabricated $\frac{\lambda}{4}$ NbN Resonators.

3.1.2 RF-SQUID

There are three main parts of the RF-SQUID designs that need to be addressed in this section: the RF-SQUID dimensions for its relevance on the device sensitivity, the junction dimensions and the mutual inductance that coupled the CPW and SQUID. They are going to be discussed following this order.

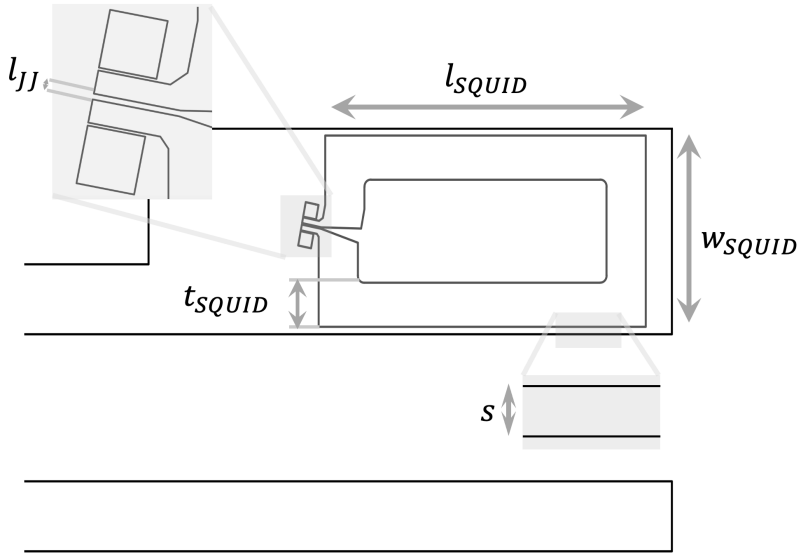

Figure 3.2: Dimensions specifications of the RF-SQUID: loop external length L_{SQUID}, loop external width w_{SQUID}, loop thickness t_{SQUID}. There are also two close up parameters, one that indicates the junction length l_{JJ} and s distance between the loop and the central line of CPW.

3.1.2.1 RF-SQUID loop

The internal area of the SQUID loop A_{loop} is a key parameter to its flux sensitivity. When A_{loop} is increased, it leads to higher flux sensitivity, however it increases the loop inductance L_{loop} which in its turn increases the screening parameter $\beta_{RF,LC}$. It has to be kept in mind that for the purpose of the experiment the interest is to maintain $\beta_{RF,LC} \ll 1$ and be in its linear regime, Section 2.1.3.
In our design the A_{loop} was aimed to be 100 µm^2, however, as the nanoribbon position does not always have to be straight the final area may vary. The RF-SQUID loop parameters for each resonator can be seen in Table 3.3.

Component		Resonator $l^L_{\lambda/4} = 36\,\text{mm}$	Resonator $l^R_{\lambda/4} = 30\,\text{mm}$
External loop length	l_{loop}	25 µm	27 µm
External loop width	w_{loop}	13 µm	12 µm
Loop thickness	t_{loop}	3 µm	3 µm
Internal Area	A_{loop}	133 µm^2	126 µm^2

Table 3.3: Geometric parameters of the RF-SQUID loops designed.

3.1.2.2 RF-SQUID junction

The last relevant parameters to comment on the RF-SQUID design is the Josephson Junction dimensions. The junctions, in order to reduce the number of current modes in the nanoribbon as seen in Section 2.2.2, were selected to have a thickness t_{JJ} inferior than 20 nm with a junction width w_{JJ} less than 100 nm. These two parameters are indicated as an approximation as they depend on the nanowire characteristics. The only parameter that could be controlled on design was the junctions length l_{JJ}, as it depended on the electrodes distance, and it was chosen to be of 100 nm.

3.1.3 Estimation of the mutual inductance

As seen in Figure 2.10 the coupling between the $\lambda/4$ CPW resonator and RF-SQUID depends on the mutual inductance between resonator and loop. The mutual inductance can be estimated approximating CPW to a wire as the central line of the resonator has the highest current density [8], [24]:

$$M = \frac{\mu_0}{2\pi} l_{SQUID} \ln \frac{s + w_{SQUID}}{s} \tag{3.1}$$

where μ_0 is the vacuum permeability, l_{SQUID} is the loop external length, w_{SQUID} is the loop width and s the distance between the loop and CPW central line. Given an s of 0.5 µm, for the left resonator RF-SQUID, this equation gave a mutual inductance of 20 pH. However, Sonnet simulations lowered the value to 16 pH.

3.2 Devices Nanofabrication

The following section describes the nanofabrication process of the devices.

3.2.1 Nanofabrication process

The overall device fabrication consists of four lithography processes. First, the $\frac{\lambda}{4}$ NbN Resonators were patterned onto sapphire substrates. The second process comprises engraving a window pattern to protect the resonator when stamping the Bi_2Se_3 nanoribbon. The third process corresponds to fabricating two gold pads to clamp the selected nanoribbon, and finally do a forth lithography to embbed the TI in a aluminium RF-SQUID loop. In the following sections there is an insight of each lithography process.

3.2.1.1 Lithography I. Pattern $\frac{\lambda}{4}$ NbN Resonators

The first lithography process patterned the $\frac{\lambda}{4}$ NbN resonators. The overall etching lithography is showed in Figure 3.3 from left to right, it starts with a 5 mm × 5 mm sapphire substrate with 100 nm layer of sputtered NbN. Afterwards, 450 nm of PMMA A6 was span and soft-baked at 170 °C. The pattern was then tranferred using Electron Beam Lithography (EBL) and, once developed, etched via reactive ion etching (RIE) using an argon and chloride mix .

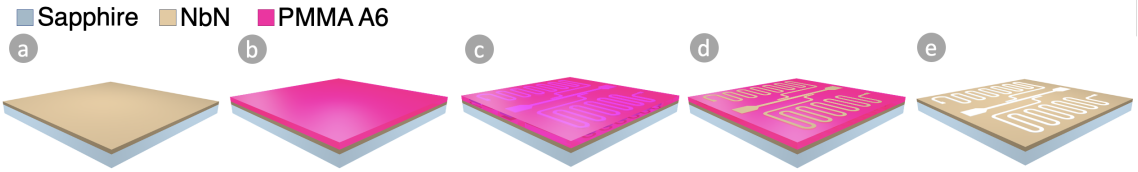

Figure 3.3: Process flow for patterning $\frac{\lambda}{4}$ NbN resonators: (a) Sapphire substrate with sputtered NbN thin film. (b) Span PPMA A6 single layer. (c) EBL exposed pattern of the resonators. (d) Developed device before etching. (e) Patterned $\frac{\lambda}{4}$ NbN resonators.

3.2.1.2 Lithography II. Pattern a window in the SQUID area

The method chosen to transfer the nanoribbons was stamping, therefore to avoid shorting the resonator due to misplaced nanoribbons, this second lithography was designed. The lithography consists of spinning a 160 nm of MMA8 EL6 with a softbake of 130 °C and then to pattern a 100 µm by 100 µm window around the SQUID area via EBL. As the objective of this process is just the window pattern, no more steps are required after development.

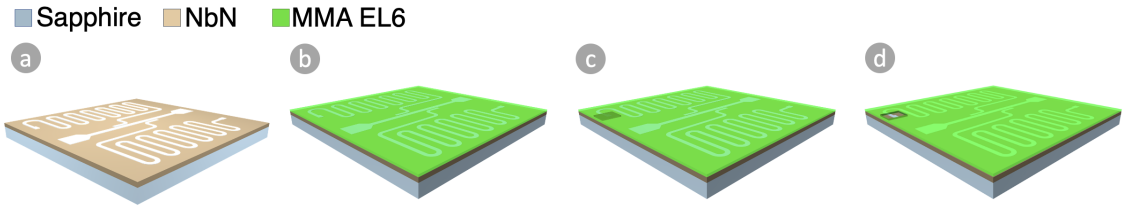

Figure 3.4: Fabrication to pattern a window in the SQUID area: (a) Patterned $\frac{\lambda}{4}$ NbN resonators. (b) A single layer of MMA8 EL6 is spun. (c) Device with the EBL exposed window (d) Final result of the MMA8 EL6100 µm by 100 µm window patterned on the device.

3.2.1.3 Lithography III. Clamping the Bi_2Se_3 nanoribbons with gold pads

Once a nanoribbon of thickness inferior 100 nm is transferred onto the SQUID area, the next step is to clamp it. Figure 3.5 illustrates the clamping process that avoids the nanoribbon to move when the SQUID is patterned.

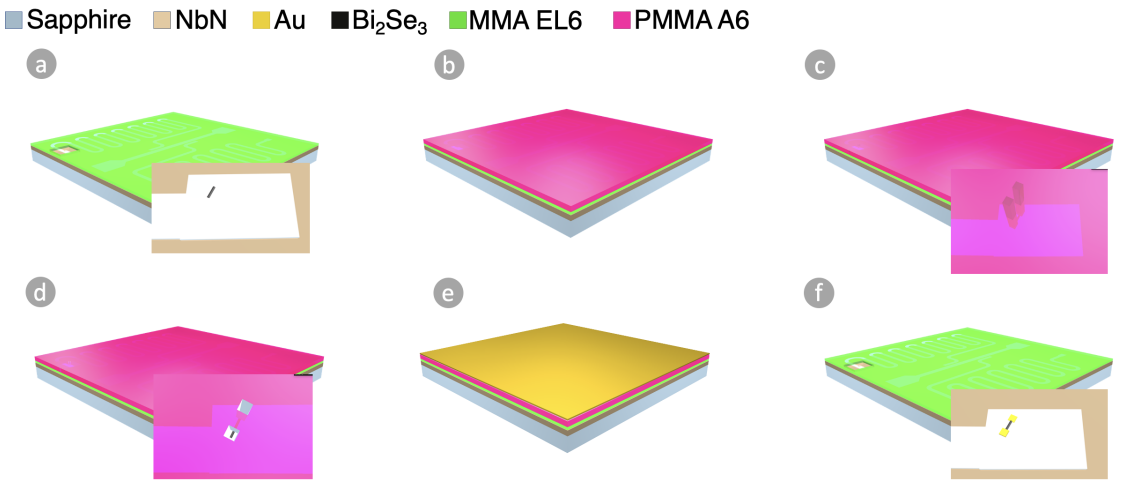

Figure 3.5: Schematic sketch of the gold nanopads patterning: (a) (b) Single 450 nm single layer of PMMA A6. (c) Exposure through EBL of the gold nanopads pattern. (d) Gold pads pattern developed. (e) Deposition of a Ti/Au thin film. (f)Result of the gold pads to clamp the nanoribbon.

Showed in Figure 3.5 (b) a 450 nm PPMA A6 layer is span and soft-baked at 130 °C an inferior temperature that in the first lithography due to the degradation of Bi_2Se_3 at higher temperatures (introducing Se vacancies). Afterwards, two gold pads of size

1 µm × 1 µm are patterned through EBL and, once developed, a 5 nm Ti layer is evaporated, for adhesion purposes, and then 40 nm of gold. Using a different resist from 3.2.1.2, the window pattern, also allows to remove the new PMMA A6 layer while keeping the MMA8 EL6 resist. Notice also, that it is important to avoid sonication during the resist removal to prevent that the nanoribbon detaches from the substrate.

3.2.1.4 Lithography IV. RF-SQUID Pattern

The last lithography step refrains to pattern an aluminium RF-SQUID interrupted by the TI junction. As stated in the last chapter, the fabricated Josephson Junction aims to have 100 nm length. It can be seen in Figure 3.6 that in terms of nanofabrication, this translates to the use of a trilayer recipe, where the resolution is determined by the center resist, a 90 nm layer of ARP 1:2. The other resists spun were 160 nm layer of MMA8 EL6 and 450 nm layer of PMMA A6. All resists were soft-baked at 130 °C. Following [25], [26], after 60 s development for each resist, 4 nm of Pt and 100 nm of Al were deposited through thermal evaporation.

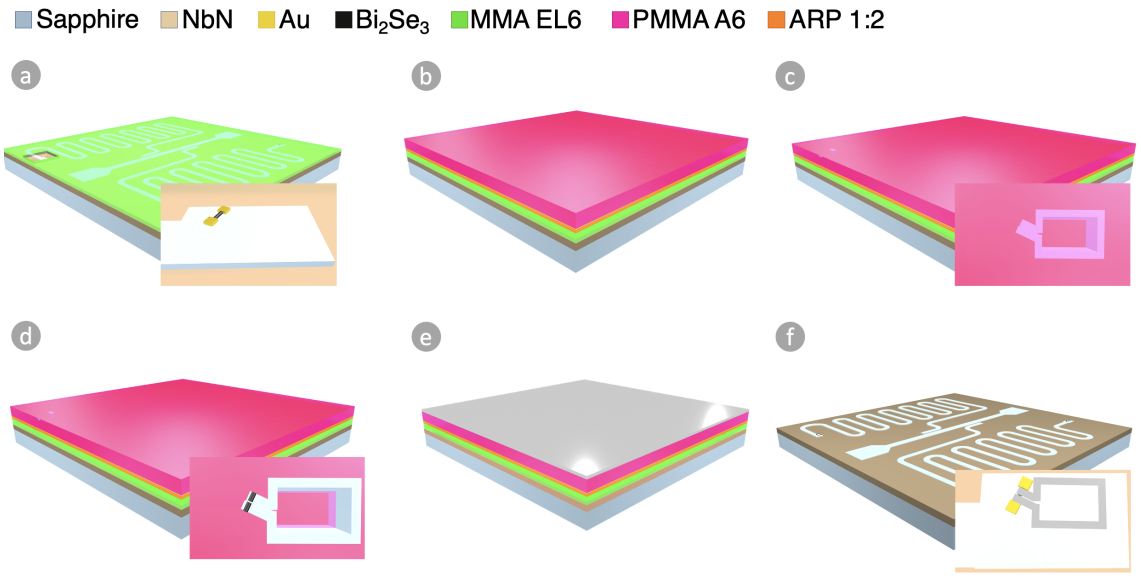

Figure 3.6: Illustration of the process employed to pattern the SQUIDs: (a) Bi_2Se_3 nanoribbon clamped with two gold pads. (b) Trilayer recipe of 160nm of MMA EL6, then 60nm of ARP 1:2 and later 450nm of PMMA A6. (c) RF-SQUID pattern exposure by EBL. (d) Pattern development. (e) Deposition of 4 nm of Pt and 100 nm of Al. (f) Schematic result of two Al RF-SQUID loops with a Bi_2Se_3 weak links coupled to $\frac{\lambda}{4}$ NbN resonators.

3.2.2 Final Device

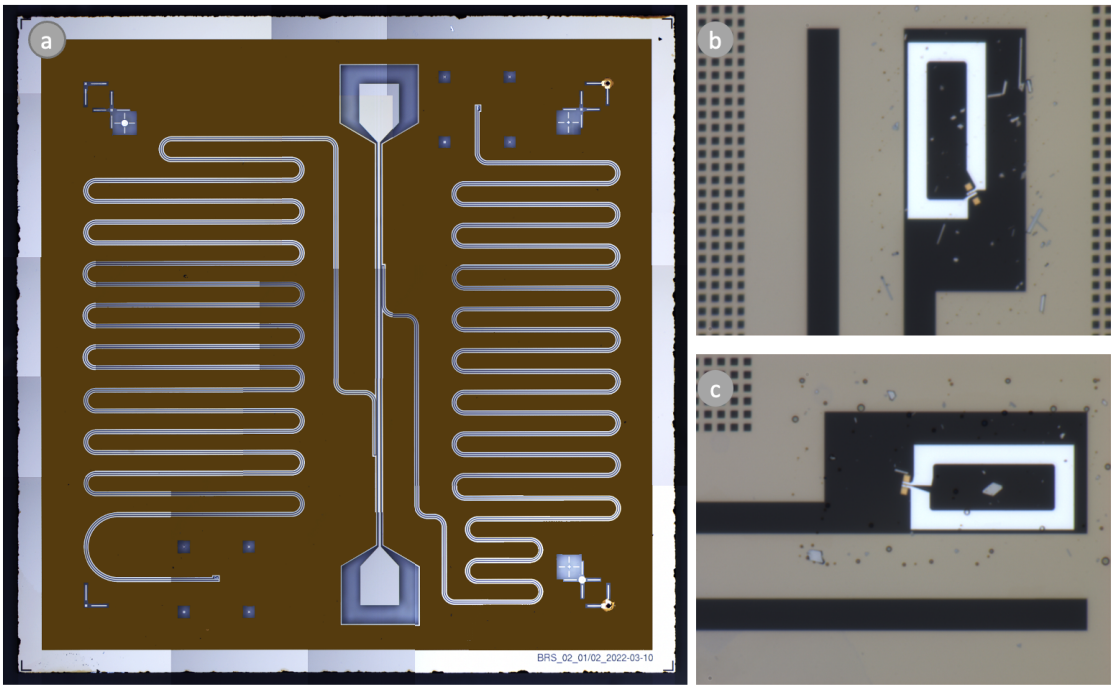

Figure 3.7: Optical microscope image of the nanofabricated device. (a) False colored of the device. (b) Aluminum RF-SQUID coupled to the right resonator. (c) Aluminium RF-SQUID coupled to the left resonator.

The overall device can be seen in the false-colored Optical Microscope (OM) picture depicted in Figure 3.7a. Figure 3.7b shows a close up of the left aluminium RF-SQUID resonator and Figure 3.7c the one for the left. In these last OM pictures misplaced nanoribbons can also be observed.

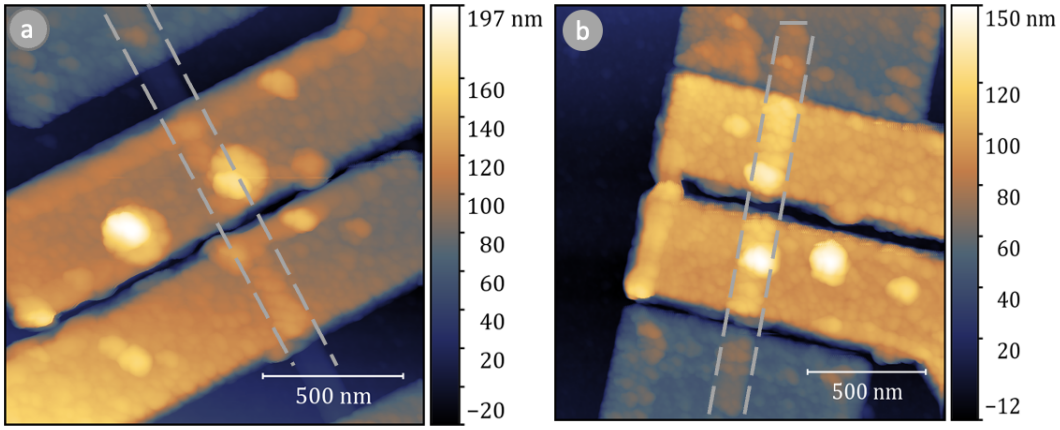

Figure 3.8: AFM images of the RF-SQUID junction where the TI nanoribbon is distinguished with a grey discontinuous line. (a) Nanoribbon of thickness $t = 16\,\text{nm}$ embedded in the RF-SQUID coupled to the right resonator in Figure 3.7b. (b) Nanoribbon of thickness $t = 19\,\text{nm}$ embedded in the RF-SQUID coupled to the left resonator Figure 3.7c.

Details of the aluminum RF-SQUIDs Josephson Junctions can be observed through Atomic Force Microscope (AFM) images in Figure 3.8, corresponding Figure 3.8(a) to the RF-SQUID in Figure 3.7(b) and Figure 3.8(b) to the RF-SQUID in Figure 3.7(c). The nanoribbons of both junctions are indicated with a discontinuous grey line, being the one in Figure 3.8(a) of thickness $t_{JJ} = 19\,\text{nm}$ and the one in Figure 3.8(b) of thickness $t_{JJ} = 16\,\text{nm}$.
Note that the junction in Figure 3.8(b) appears to be shorted, however it was confirmed through measurement data that it is not. What appears to be a short in the junction is probably because the AFM tip could not map accurately the weak link as the length is roughly 100 nm. This hypothesis could have been confirmed through Scanning Electron Microscope (SEM), however the measurement was not performed to avoid surface charging that would have caused doping the nanoribbon.

3.3 Characterization

This section contemplates all relevant parts of the devices characterization. It comprises the experimental set up description and the experiments performed which include a power response analysis of the system. It also explains the experimental data fitting considerations to obtain the fundamental frequency and quality factor variation of the resonator and concludes with the simulation model realized to support the characterization.

3.3.1 Experimental Set Up and measurement

The experimental set up to probe the device susceptibility can be seen in Figure 3.9. The circuit was mounted on a dilution refrigerator cryostat from Oxford Instruments which is a commonly used device that allows to reach 20 mK temperature regime using a mixture of two Helium isotopes, He^3 and He^4. In particular, the cryostat used in the measurements was equipped with a magnetic field shield that protected the system from environment magnetic fluctuations. Furthermore, as three devices were measured in the same cool down, each device was protected by their own magnetic shield.
To obtain the different sets of data, we set up the mixing chamber, represented in Figure 3.9 below the 2 K stage, at a temperature between 20 mK and 1000 mK. A Vector Network Analyzer (VNA) was connected at the input and output signal ports at room temperature, which allowed this instrument to characterize the transmitted and reflected signal across a band gap of interest. In particular, the parameter used to further analyse the measurements was the reflexion coefficient, Γ_r. Furthermore, the VNA also allowed to determine a specific measurement power, in particular data was obtained at 0 dB and -5 dB, further details are provided in the next section.
Send from VNA Port 1 the microwave signal had centered frequency of one of the resonator harmonics, frequencies at Table 3.2, and went down to through a set of attenuators which reduced the input signal thermal noise. These attenuators were mounted at different stages of the dilution refrigerator according to thermalization power of each stage [27]. At the mixing chamber the signal reached the device, represented by a yellow square in Figure 3.9, that was biased through a magnet coil.

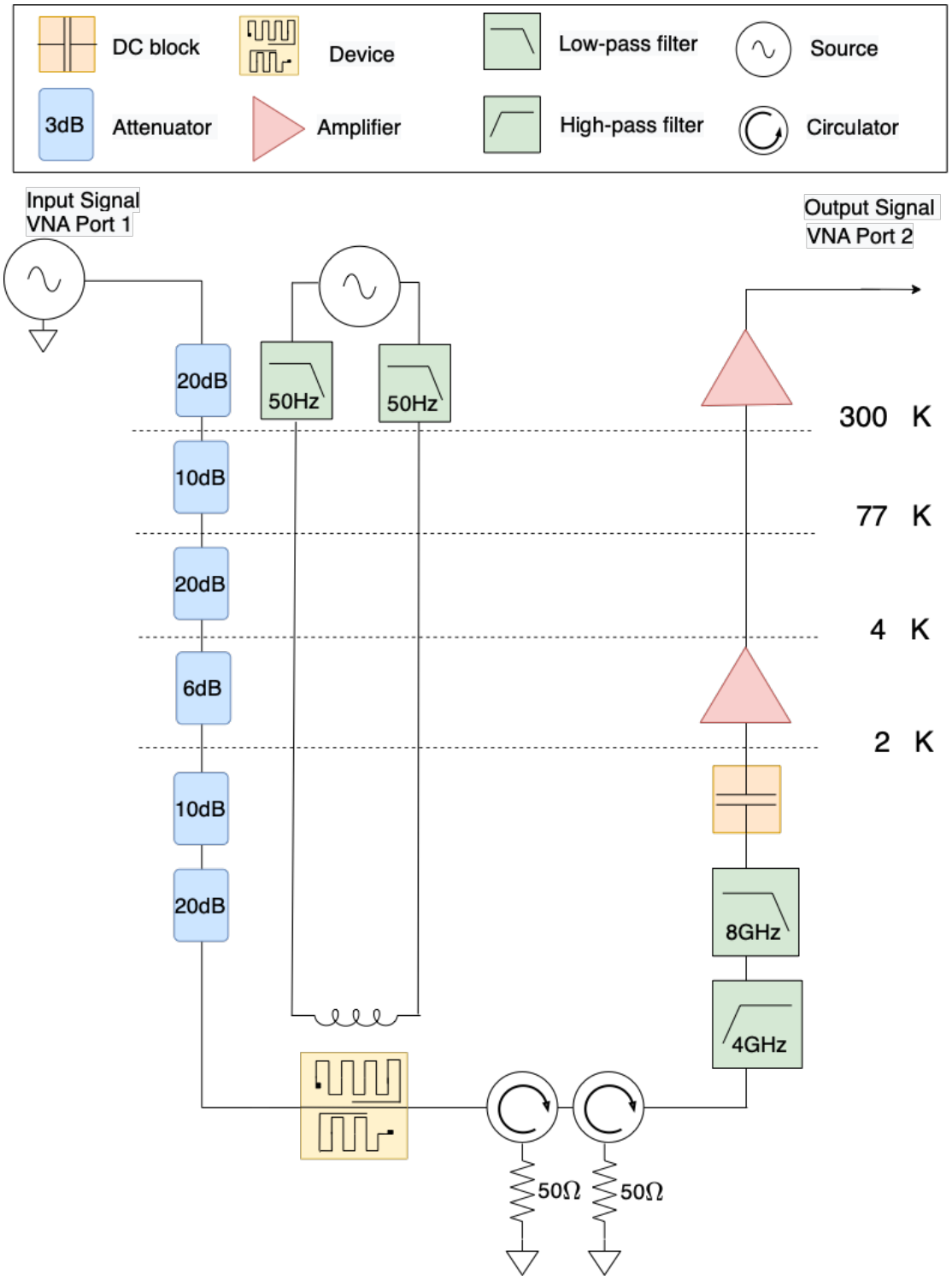

Figure 3.9: Sketch of the experimental set up. The signal is send from a microwave source at room temperature to the refrigerator and transmitted down to 10 mK through a set of attenuators. At the mixing chamber the signal reaches the device, that is biased through a coil magnet, and passes through two circulators. Afterwards, the signal is filtered through a 4 GHz high-pass filter and a 8 GHz low-pass filter before reaching the low temperature amplifier at the 5 K stage and to the VNA. A second amplifier is placed at room temperature.

The signal for the magnet coil was send from room temperature through a set of RC filters with cutoff frequency below 50 Hz to filter the dc-bias of the signal. Once the signal was transmitted through the device, it went through two circulators, that discriminated the signal up to its propagation direction. Afterwards, the signal was filtered through a 4 GHz high-pass filter and a 8 GHz low-pass filter as the low temperature amplifier at the 5 K stage has a band-pass between those frequencies. Another amplifier was incorporated at room temperature to the circuit before the signal reached the VNA Port 2.

3.3.1.1 Power response analysis

A power response analysis was carried in order to obtain the best S/N ratio in the measured data. As mentioned, the two powers chosen were 0 dBm to −5 dBm. However, effectively, the fridge experienced a variation of 15 dBm, going from −40 dBm to −25 dBm as the room temperature attenuator in Figure 3.9 for the first measurement was of −40 dBm, instead of −20 dBm.
For a further analysis, the number of photons for each power can be obtained using

$$N = \frac{P_c}{h f_n^2} \tag{3.2}$$

where h is the Planck constant and f_n the resonance frequency and P_c is the circulating power. To calculate P_c, one can use the following expression:

$$P_c = P_{in} \frac{Q_{int}^2 Q_{ext}}{\pi (Q_{int} + Q_{ext})^2} \tag{3.3}$$

Here, P_{in} is the power that goes inside the device, Q_{int} is the internal quality factor and Q_{ext} is the external quality factor which are obtained through data fitting the measurements data sets.

3.3.2 Experimental data fitting

For a given power, the data sets were taken for a temperature range between 20 mK and 1000 mK, sweeping around the center frequency f_n while biasing the coil current φ. Therefore, through the VNA, one obtains the reflexion coefficient Γ_r for a given temperature T as a function of f, φ which can be fitted as:

$$\Gamma_r(f, \varphi) = |\Gamma_{r0}| e^{-2\pi i f \tau_d} \left(1 - \frac{Q_{tot}}{Q_{ext}} \frac{e^{i\varphi_0}}{1 + 2iQ_{tot} \frac{f - f_n}{f_n}} \right) \tag{3.4}$$

where Γ_{r0} is a given amplitude, τ_d expresses a signal delay, φ_0 reflects on a rotation, Q_{tot} is the total quality factor, Q_{ext} is the external quality factor and f_n is the resonance frequency. Through equation (3.4) one can identify the frequency variation $\delta f / f_n$ as:

$$\frac{\delta f}{f_n} = \frac{f - f_n}{f} \tag{3.5}$$

which is proportional to the real susceptibility component χ' through equation (2.29) where $\omega = 2\pi f$. Instead, the imaginary susceptibility term χ'' relates to variation

of the quality factor, $\delta(1/Q)$ that is contained in the internal quality factor Q_{int}. Considering that through equation (3.4) one can obtain Q_{tot} and Q_{ext}, the Q_{int} can be calculated through equation (2.26).
The quality factor variation $\delta(1/Q)$ reflects on the dissipative response of the STIS junction having as contributions the diagonal χ_D and non-diagonal χ_{ND} susceptibility components. As seen in Section 2.2.3, χ_D and χ_{ND} are frequency dependant, so their contributions will vary with the probing frequency f. Particularly, at high temperatures and low frequencies $\delta(1/Q)$ is expected to be dominated by χ_D, whereas at low temperatures and high frequencies is dominated by χ_{ND} [7], [19], [20]. The objective here is to obtain an estimation of the diagonal γ_D and non-diagonal γ_{ND} relaxation rates using these two frequency and temperature regimes.

3.3.3 Model of TI Susceptibility Response

To characterize the energy band structure of the TI junction, we compared the experimental data to a short ballistic junction model and subtracted the relaxation γ_D and microwave transitions γ_{ND} rates.
The model implements the behaviour of a short ballistic junction described in Chapter 2, this approximation has been taken because in previous experiments we could observe Fabry-Pérot oscillations using this material. Given a determined frequency, it takes into account the geometrical junction parameters, width w_{JJ}, length l_{JJ} and thickness t_{JJ}, and the material ones considering a critical temperature for the superconducting electrodes of aluminium and the chemical potential at the Dirac point. With these parameters, it calculates the corresponding conduction channels, equation (2.15), and the ABS energy distributions.
Then, inserting the temperature T and the chosen relaxation γ_D and microwave transitions γ_{ND} rates, it calculates the three susceptibility contributions. All the Josephson Susceptibility χ_J, equation (2.20), the diagonal susceptibility χ_D, equation (2.21) and the non-diagonal susceptibility χ_{ND}, equation (2.22) considered are calculated for every conduction channel, in other words for every τ or every individual pair of ABS, and then they are summed. In this way, we can obtain the total susceptibility of the junction and the different susceptibility components.

4

Results

The results presented in the following chapter belong to the $t_{JJ} = 19\,\text{nm}$ Bi_2Se_3 nanoribbon. Here, we first discuss the system's power response and then focus on the study of the susceptibility response.

4.1 System's behaviour at $0\,\text{dBm}$ and $-5\,\text{dBm}$ power

To characterize the power response of the circuit at $0\,\text{dBm}$ and $-5\,\text{dBm}$, this section analyses the results of quality factor variation $\delta(1/Q)$ measurements at resonance frequencies $4.40\,\text{GHz}$ and $8.16\,\text{GHz}$. The result of the $\delta(1/Q)$ measurements can be seen in Figure 4.1, where the first row are the measurements at $0\,\text{dBm}$ with (a) being the experimental data taken at $4.40\,\text{GHz}$ and (b) at $8.16\,\text{GHz}$, whereas the

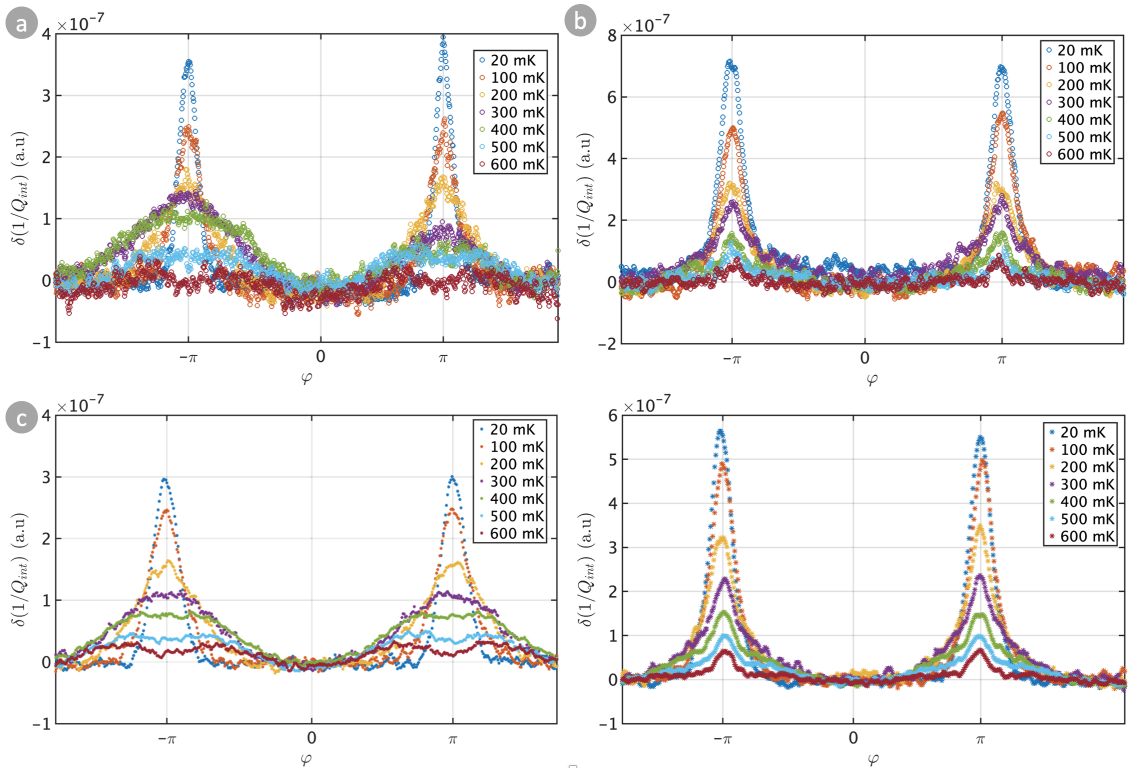

Figure 4.1: Experimental data of the quality factor variation, $\delta(1/Q)$ taken at: (a) $4.40\,\text{GHz}$ and power $0\,\text{dBm}$, (b) $8.16\,\text{GHz}$ and power $0\,\text{dBm}$, (c) $4.40\,\text{GHz}$ and power $-5\,\text{dBm}$ and $8.16\,\text{GHz}$ and power $-5\,\text{dBm}$

second row are the corresponding measurements at $-5\,\text{dBm}$ for (c) $4.40\,\text{GHz}$ and

(d) 8.16 GHz. When the power increases the S/N ratio is expected to improve as the output signal also increases in power, decreasing the background noise. Also, it saturates noise sources. The result, as observed in Figure 4.1, is a much more smoother curve for the −5 dBm signals.
The number of photons and corresponding circulating power is found in Table 4.1:

Power	f_n =4.40 GHz		f_n =8.16 GHz	
	$P_{circ}(mW)$	N	$P_{circ}(W)$	N
0 dB	$1.64 \cdot 10^{-11}$	1500	$1.93 \cdot 10^{-11}$	500
−5 dB	$2.15 \cdot 10^{-9}$	150.000	$1.99 \cdot 10^{-9}$	50.000

Table 4.1: Circulating power P_{circ} and number of photons N of measurements at frequencies 4.40 GHz and 8.16 GHz for powers 0 dBm and −5 dBm

These results are consistent with previous studies related to microwaves loses at low power in milikelvin regime carried by the group [28].

4.2 Characterization of TI energy band structure

As stated in the previous chapter, the χ is frequency and temperature dependant. Particularly, the dissipative term χ'' is expected to vary according to χ_D or χ_{ND} contributions. Therefore, to identify γ_D and γ_{ND} the results discussed in this chapter belong to the 4.40 GHz and 8.16 GHz harmonics for a two-set of temperatures. An initial evaluation of the temperature response is provided before characterizing γ_D and γ_{ND}.

4.2.1 TI susceptibility response at low and high temperatures

The following section analyses the temperature response of the TI junction for temperatures comprising 20 mK and 1000 mK taken at −5 dBm. The frequency variation $\delta f/f_n$ scans against the junction flux bias are found in Figure 4.2. Here, Figure 4.2(a) gives the result of the data measurement at 4.40 GHz and Figure 4.2(b) for 8.16 GHz. As expected, there is not a significant difference between the scan at the two frequencies, just a tendency towards the sinusoidal behaviour of this response due to equation (2.18).

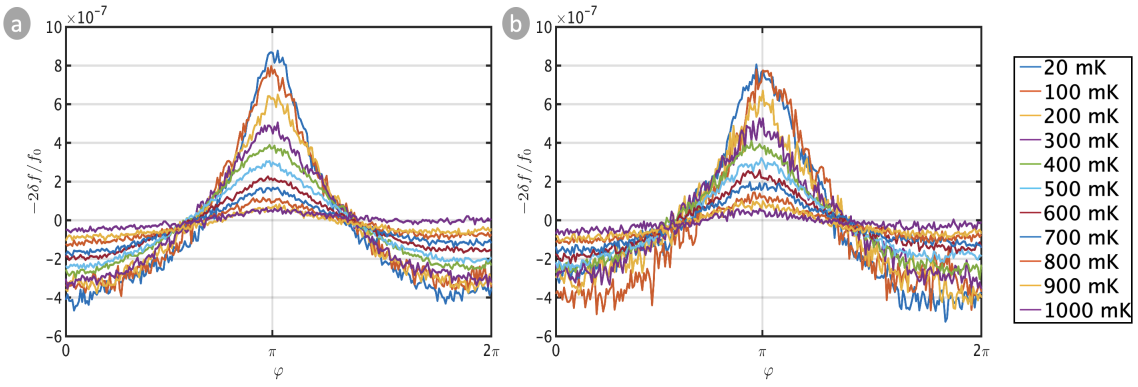

Figure 4.2: Experimental data of $-2\delta f/f_n$ plotted against the flux bias of the junction for temperatures between 20 mK to 1000 mK at −5 dBm for: (a) 4.40 GHz and (b) 8.16 GHz.

However, the dissipative response, reflected on quality factor variation $\delta(1/Q)$, shows indeed a mismatch for low and high frequencies. Figure 4.3(a) shows the result of measurements at 4.40 GHz, with a mismatch $\delta(1/Q)$ behaviour at low, from 20 mK to 400 mK, and high, from 500 mK to 1 K, temperatures. The low temperatures scans present a single peak behaviour that turns to a two-peak for the high temperatures. According to literature predictions, this indicates that for higher temperatures and lower frequencies the χ_D contribution is dominant.
For the measurements at 8.16 GHz, Figure 4.3(b), we found that $\delta(1/Q)$ presents a single-peak behaviour enhanced at low temperatures, which is in agreement with the prediction of χ_{ND} dominating.

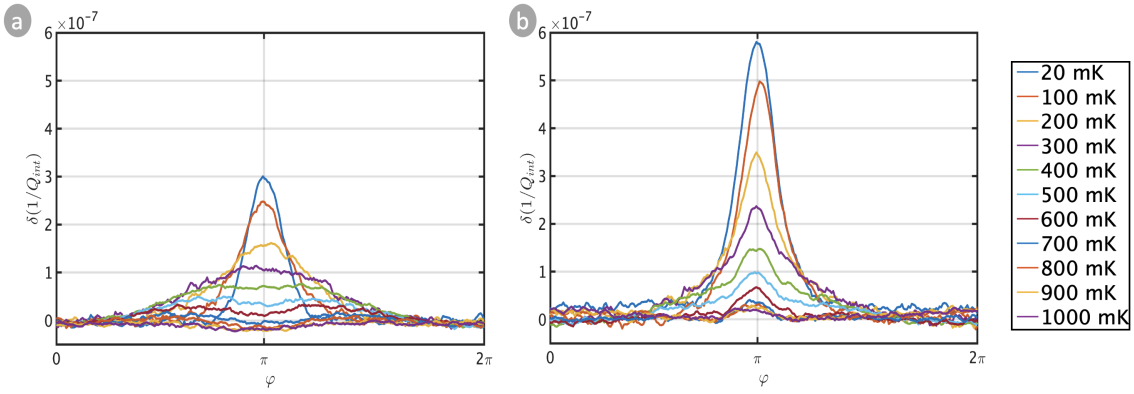

Figure 4.3: Experimental data of $\delta(1/Q)$ plotted against the flux bias of the junction for temperatures in a range from 20 mK to 1000 mK taken at −5 dBm for: (a) 4.40 GHz and (b) 8.16 GHz.

4.2.2 TI susceptibility characterization, γ_D and γ_{ND}

To perform a qualitative analysis of the TI junctions and obtain an estimate value of γ_D and γ_{ND}, this section focuses on the evaluation of the 300 mK and 500 mK temperature data sets.
Figure 4.4 shows the experimental data sets -line- and the simulated response -dashed lines- for $\delta f/f_n$ and $\delta(1/Q)$. Figure 4.4(a) illustrates the $\delta f/f_n$ results at 4.40 GHz, Figure 4.4(a), and 8.16 GHz, Figure 4.4(b). Analogously, Figure 4.4(c) depicts the data for $\delta(1/Q)$ at 4.40 GHz and Figure 4.4(d) for 8.16 GHz.
Despite the simulation model not fitting the data experiments, it reproduces the behaviour of the measurements using a $\gamma_D = 2$ GHz and $\gamma_{ND}^{4.40GHz} = 3$ GHz and $\gamma_{ND}^{8.16GHz} = 10$ GHz. Aside from implementing the TI model to a fitting programme, we argue that the high value of $\gamma_{ND}^{8.16GHz}$ can be due to two reasons. As this parameter reflects on the induced microwave transitions within the energy spectrum, we propose that the gold pads used to clamp the nanoribbon act as an ohmic bath. One possible solution would be to substitute them with aluminium, so all the nanoribbon is covered except the junction. However, there is also the possibility that the high γ_{ND} is intrinsic of the TI, generated by an oxidized layer at the surface. The only possible solution for this would be to change the material, though this route was explored using $[Bi_xSb_{1-x}]_2Te_3$ thin films obtaining too high contact resistances, in the range of 47 Ω to 100 Ω for different fabrication methods, to move on in fabrication.

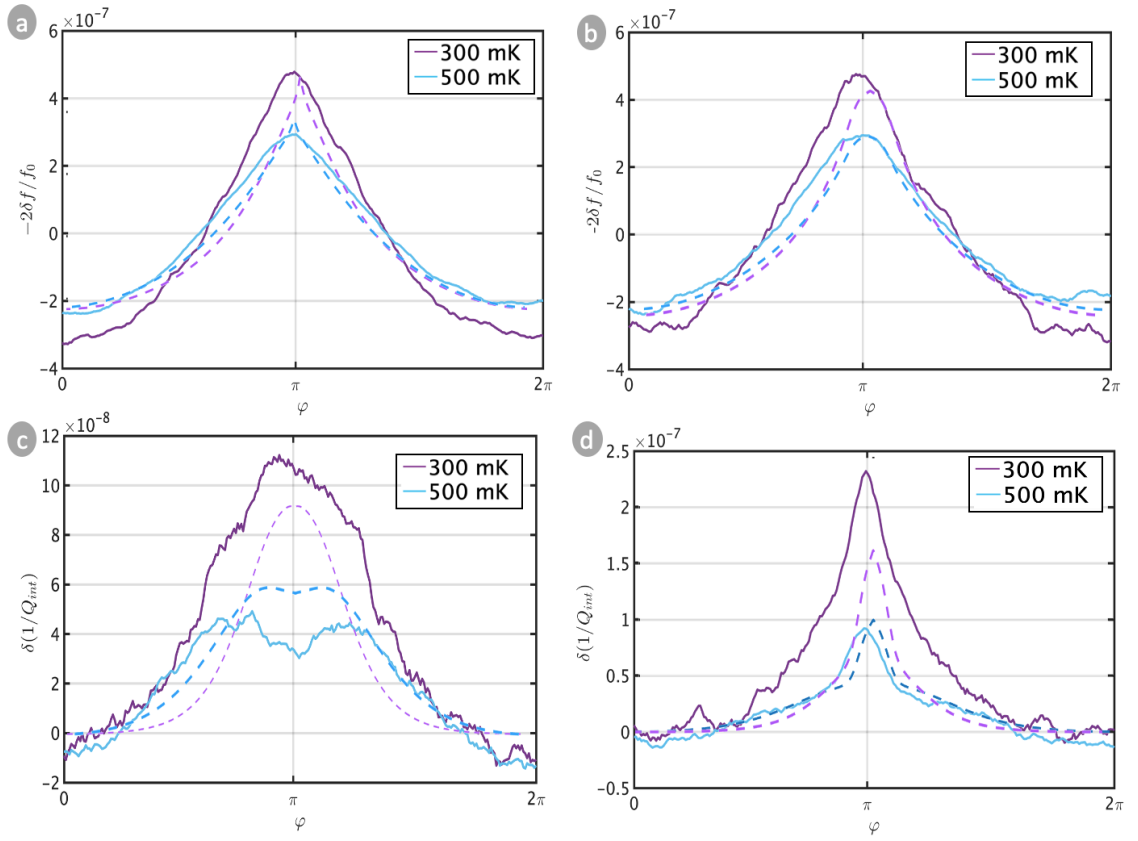

Figure 4.4: Experimental data -line- and the corresponding fitting from the model -dashed line- plots for: (a) $-2\delta f/f_n$ plotted against the flux bias of the junction for temperatures 300 mK and 500 mK at 4.40 GHz. (b) $-2\delta f/f_n$ plotted against the flux bias of the junction for temperatures 300 mK and 500 mK at 8.16 GHz. (c) $\delta(1/Q)$ plotted against the flux bias of the junction for temperatures 300 mK and 500 mK at 4.40 GHz (d) $\delta(1/Q)$ plotted against the flux bias of the junction for temperatures 300 mK and 500 mK at 8.16 GHz.

5
Conclusion

In this thesis we designed, nanofabricated and characterized a device through microwave reflectometry measurements to probe the susceptibility of a STIS junctions made from Bi_2Se_3 nanowires and aluminum electrode contacts. Through the susceptibility measurements we could study the mechanisms that drive the band structure of the TI: population relaxation and induced microwave transitions. In fact, when the experimental data was compared to a short ballistic junction model, we were able to identify the relaxation and microwave transition rates.
There are different directions to take in this project. In the nanofabrication regards, if we continue using the same TI material, the next step is to replace the gold pads to clamp the nanowire by aluminium, disabling a possible ohmic source. It will also be interesting to modify the RF-SQUID design and include a gate to be able to tune the Dirac point of the material. However, there is the option to go back to use $[Bi_xSb_{1-x}]_2Te_3$ thin films. In this case, the next step is to continue exploring the different routes of the thin film contacts to lower the contact resistance. As for data processing, the short ballistic junction model proposed should be implemented to a fitting model to characterize finely the experimental data.

Bibliography

[1] H. Zhang, C.-X. Liu, X.-L. Qi, X. Dai, Z. Fang, and S.-C. Zhang, "Topological insulators in bi2se3, bi2te3 and sb2te3 with a single dirac cone on the surface," *Nature physics*, vol. 5, no. 6, pp. 438–442, 2009.

[2] L. Fu and C. L. Kane, "Superconducting proximity effect and majorana fermions at the surface of a topological insulator," *Physical review letters*, vol. 100, no. 9, p. 096 407, 2008.

[3] J. P. Heremans, R. J. Cava, and N. Samarth, "Tetradymites as thermoelectrics and topological insulators," *Nature Reviews Materials*, vol. 2, no. 10, pp. 1–21, 2017.

[4] Y. Ando, "Topological insulator materials," *Journal of the Physical Society of Japan*, vol. 82, no. 10, p. 102 001, 2013.

[5] P. de Gennes, "Boundary effects in superconductors," *Reviews of Modern Physics*, vol. 36, no. 1, p. 225, 1964.

[6] J. Andzane, G. Kunakova, S. Charpentier, *et al.*, "Catalyst-free vapour–solid technique for deposition of bi 2 te 3 and bi 2 se 3 nanowires/nanobelts with topological insulator properties," *Nanoscale*, vol. 7, no. 38, pp. 15 935–15 944, 2015.

[7] B. Dassonneville, "Dynamics of andeev states in a normal metal-superconductor ring: Supercurrent fluctuations and spectroscopy of the minigap," Ph.D. dissertation, Paris 11, 2014.

[8] R. Haller, "Probing the microwave response of novel josephson elements," Ph.D. dissertation, Universität Basel, 2021.

[9] B. Josephson, "The discovery of tunneling supercurrents," *Science*, vol. 184, no. 4136, pp. 527–530, 1974.

[10] P. W. Anderson and J. M. Rowell, "Probable observation of the josephson superconducting tunneling effect," *Physical Review Letters*, vol. 10, no. 6, p. 230, 1963.

[11] P. Krantz, A. Bengtsson, M. Simoen, *et al.*, "Single-shot read-out of a superconducting qubit using a josephson parametric oscillator," *Nature communications*, vol. 7, no. 1, pp. 1–8, 2016.

[12] A. Andreev, "Thermal conductivity of the intermediate state of superconductors ii," *Sov. Phys. JETP*, vol. 20, p. 1490, 1965.

[13] C. Beenakker, "Universal limit of critical-current fluctuations in mesoscopic josephson junctions," *Physical review letters*, vol. 67, no. 27, p. 3836, 1991.

[14] F. Tafuri, *Fundamentals and frontiers of the Josephson effect*. Springer Nature, 2019, vol. 286.

[15] C.-X. Liu, X.-L. Qi, H. Zhang, X. Dai, Z. Fang, and S.-C. Zhang, "Model hamiltonian for topological insulators," *Physical Review B*, vol. 82, no. 4, p. 045 122, 2010.

[16] C. Li, J. C. de Boer, B. de Ronde, *et al.*, "4π-periodic andreev bound states in a dirac semimetal," *Nature materials*, vol. 17, no. 10, pp. 875–880, 2018.

[17] J. Tworzydło, B. Trauzettel, M. Titov, A. Rycerz, and C. W. Beenakker, "Sub-poissonian shot noise in graphene," *Physical review letters*, vol. 96, no. 24, p. 246 802, 2006.

[18] G. Kunakova, A. P. Surendran, D. Montemurro, *et al.*, "Topological insulator nanoribbon josephson junctions: Evidence for size effects in transport properties," *Journal of Applied Physics*, vol. 128, no. 19, p. 194 304, 2020.

[19] B. Dassonneville, A. Murani, M. Ferrier, S. Guéron, and H. Bouchiat, "Coherence-enhanced phase-dependent dissipation in long sns josephson junctions: Revealing andreev bound state dynamics," *Physical Review B*, vol. 97, no. 18, p. 184 505, 2018.

[20] A. Murani, B. Dassonneville, A. Kasumov, *et al.*, "Microwave signature of topological andreev level crossings in a bismuth-based josephson junction," *Physical Review Letters*, vol. 122, no. 7, p. 076 802, 2019.

[21] M. Ferrier, B. Dassonneville, S. Guéron, and H. Bouchiat, "Phase-dependent andreev spectrum in a diffusive sns junction: Static and dynamic current response," *Physical Review B*, vol. 88, no. 17, p. 174 505, 2013.

[22] M. Göppl, A. Fragner, M. Baur, *et al.*, "Coplanar waveguide resonators for circuit quantum electrodynamics," *Journal of Applied Physics*, vol. 104, no. 11, p. 113 904, 2008.

[23] P. Krantz, *The Josephson parametric oscillator–From microscopic studies to single-shot qubit readout*. Chalmers Tekniska Hogskola (Sweden), 2016.

[24] C. Janvier, "Coherent manipulation of andreev bound states in an atomic contact," Ph.D. dissertation, Université Paris-Saclay, 2016.

[25] G. Kunakova, T. Bauch, E. Trabaldo, J. Andzane, D. Erts, and F. Lombardi, "High transparency bi2se3 topological insulator nanoribbon josephson junctions with low resistive noise properties," *Applied Physics Letters*, vol. 115, no. 17, p. 172 601, 2019.

[26] S. Charpentier, L. Galletti, G. Kunakova, *et al.*, "Induced unconventional superconductivity on the surface states of bi2te3 topological insulator," *Nature communications*, vol. 8, no. 1, pp. 1–8, 2017.

[27] S. Krinner, S. Storz, P. Kurpiers, *et al.*, "Engineering cryogenic setups for 100-qubit scale superconducting circuit systems," *EPJ Quantum Technology*, vol. 6, no. 1, p. 2, 2019.

[28] M. Arzeo, F. Lombardi, and T. Bauch, "Microwave losses in mgo, laalo3, and (la0. 3sr0. 7)(al0. 65ta0. 35) o3 dielectrics at low power and in the millikelvin temperature range," *Applied Physics Letters*, vol. 104, no. 21, p. 212 601, 2014.

DEPARTMENT OF SOME SUBJECT OR TECHNOLOGY
CHALMERS UNIVERSITY OF TECHNOLOGY
Gothenburg, Sweden
www.chalmers.se

CHALMERS
UNIVERSITY OF TECHNOLOGY